

Article

Mechanical Behavior of Special-Shaped Reinforced Concrete Composite Columns Encased with GFRP Core Columns

Jing Ji ^{1,2}, Jiaqi Li ¹, Liangqin Jiang ^{1,2,*}, Hongguo Ren ^{3,*}, Qingqin Wang ⁴, Xue Wang ^{3,*}, Lingjie He ¹ and Zhanbin Zhang ¹

¹ Heilongjiang Key Laboratory of Disaster Prevention, Mitigation and Protection Engineering, Northeast Petroleum University, Daqing 163319, China

² China-Pakistan Belt and Road Joint Laboratory on Smart Disaster Prevention of Major Infrastructures, Southeast University, Nanjing 211189, China

³ Handan Key Laboratory of Building Physical Environment and Regional Building Protection Technology, School of Architecture and Art, Hebei University of Engineering, Handan 056038, China

⁴ China Academy of Building Research Co., Ltd., Beijing 100013, China

* Correspondence: jiangliangqin@nepn.edu.cn (L.J.); renhongguo@hebeu.edu.cn (H.R.); xuewang202209@163.com (X.W.)

Abstract: In order to investigate the mechanical behavior of special-shaped reinforced concrete composite columns encased with GFRP core columns (EGCSSCs) subjected to axial load, twenty-seven full-scale EGCSSCs were designed with varying parameters: axial compressive strength of core concrete (f_{cc}), axial compressive strength of peripheral concrete (f_{co}), thickness of GFRP tube (t_{gfrp}), ratio of longitudinal reinforcement (ρ_v), stirrup ratio (ρ_s) and GFRP ratio in the cross-section (α). The three-dimensional finite element refined models of EGCSSCs were established by ABAQUS finite element software, and the response of EGCSSCs under axial load was studied based on the verification of finite element modeling. The influence of different parameters on the ultimate axial compressive strength (N_{us}), initial stiffness (K), and ductility index (μ) of EGCSSCs was obtained, and the typical failure mode of EGCSSCs was clearly described. The results showed that the main failure mode of the EGCSSCs subjected to axial load was bulging outward at the middle of the EGCSSCs, showed yielding of the longitudinal steel bars, and was crushing both ends of the peripheral concrete. When the column was damaged, the peripheral concrete reached peak stress earlier than the core concrete. All specimens exhibited excellent load-carrying capacity and good ductility. Moreover, with the existence of GFRP core columns, the N_{us} and μ of the columns were increased by 11.61% and 140.86%. In addition, K increased with the increase in f_{cc} , f_{co} , t_{gfrp} and α , and the largest increments were 23.99%, 50.54%, 21.77%, and 34.19%, respectively. μ decreased with the increase in f_{cc} and f_{co} , which decreased by 14.05% and 40.28%, respectively. By using statistical regression and introducing the constraint effect coefficients and the reduction coefficient, the calculation formula for the axial compression-bearing capacity of EGCSSCs was derived, which could lay a foundation for the popularization and application of this kind of composite column in practical engineering.

Keywords: special-shaped columns; GFRP core column; constitutive model; axial load; bearing capacity



Citation: Ji, J.; Li, J.; Jiang, L.; Ren, H.; Wang, Q.; Wang, X.; He, L.; Zhang, Z. Mechanical Behavior of Special-Shaped Reinforced Concrete Composite Columns Encased with GFRP Core Columns. *Buildings* **2022**, *12*, 1895. <https://doi.org/10.3390/buildings12111895>

Academic Editor: Marco Di Ludovico

Received: 5 October 2022

Accepted: 3 November 2022

Published: 5 November 2022

Publisher's Note: MDPI stays neutral with regard to jurisdictional claims in published maps and institutional affiliations.



Copyright: © 2022 by the authors. Licensee MDPI, Basel, Switzerland. This article is an open access article distributed under the terms and conditions of the Creative Commons Attribution (CC BY) license (<https://creativecommons.org/licenses/by/4.0/>).

1. Introduction

Special-shaped reinforced concrete (RC) columns can not only increase indoor space but can also avoid frame columns protruding outward because the column limbs are hidden in the wall [1]; therefore, special-shaped RC columns are widely used in construction projects. With the development of building structures to super high-rise, heavy load, and large spans, conventional special-shaped RC columns cannot meet the strength and stiffness requirements of the structure well; thus, it is extremely urgent to propose a novel kind of special-shaped reinforced concrete composite column. Fiber-reinforced polymers (FRP) have been widely used to strengthen different concrete components, such as beams, plates

and columns [2–5], which can significantly improve the bending, tensile and interlaminar shear strength of the reinforced objects [6]. Moreover, composite materials have been widely used in the construction of subway support brackets, and the lifetime of the support brackets can be significantly improved by the application of composite materials [7,8]. Glass fiber-reinforced polymer (GFRP) tubes are composed of composite materials and have the advantages of excellent tensile performance in the circumferential direction, good corrosion resistance ability, eminent constraint effect on encased concrete and light self-weight; thus, the organic combination of concrete-filled GFRP tubes and the special-shaped columns can effectively improve the bearing capacity and stiffness of the composite columns [9]. Based on this, a novel kind of special-shaped reinforced concrete composite column encased with GFRP core columns (EGCSSCs) is proposed. The transversal deformation of the core concrete can be significantly reduced by the constraint of GFRP, and the failure of the external reinforced concrete can also be delayed [10–13]. The new kind of composite columns will be widely applied to the special-shaped frame structures [14].

The research on the mechanical properties of special-shaped columns and GFRP-confined concrete columns has become a popular topic for scholars. From 2018 to 2020, a series of experimental studies on triangular, 1/4 circular, semi-circular, fan-shaped, D-shaped, L-shaped, and T-shaped concrete-filled steel tubular (CFST) columns were carried out by Han et al. [15,16] and Liu et al. [17,18]. The results showed that the failure modes of special-shaped columns with triangular, fan-shaped, D-shaped, 1/4 circular and semi-circular under axial load were similar to those of circular, square and rectangular hollow CFST columns, and the corresponding calculation formulas of the compressive- and flexural-bearing capacity of the special-shaped CFST columns were established. The experiments on the seismic behavior of twelve steel-reinforced concrete L-shaped columns under compression–bending–shear–torsion combined action were conducted by Chen et al. [19], and the influences of variables on the failure modes, hysteretic curves, ductility, stiffness degradation and energy dissipation of the composite columns were compared and analyzed. In 2021, Hassam et al. [20] conducted experimental and numerical analyses of cross-shaped stub CFST under axial compression, and the rationality of the finite element modeling (FEM) method was verified by existing experiments, the influence regularity of different parameters on the axial compression behavior of the composite columns was obtained, and finally, the calculation equation for axial compression-bearing capacity was derived relying on the constitutive theoretical model of the constrained concrete. Tests and simulations on seven L-shaped steel–concrete composite columns under axial load were conducted by Wang et al. [21], and a theoretical model was proposed to calculate the axial strength; then, the simplified formula for determining the axial strength was derived based on the FEM and the theoretical model. From 2018 to 2022, a series of numerical analyses on the mechanical properties of H-shaped honeycombed steel web composite members with rectangular CFST flanges were carried out by Ji et al. [22–25], and the nonlinear buckling load, eccentric compression-bearing capacity formula and the restoring force models of this kind of column were established. An experimental study on the axial compression performance of cross-shaped and L-shaped multi-cavity CFST special-shaped column (CFSTSSC) was carried out by Li et al. [26], and according to the limit equilibrium theory, equations for calculating the ultimate bearing capacity of the composite columns were proposed.

A large number of experimental studies on FRP-confined concrete composite columns were successively conducted by many scholars [27]. In 2017, an experimental study on the dynamic behavior of 24 concrete columns confined by both GFRP tube and steel spiral reinforcement (GFRP-SR) under impact loadings was carried out by Huang et al. [28], and the results showed that the failure pattern of this hybrid structure was highly dependent on the level of impact energy, and increasing the tube thickness and steel spiral reinforcement volumetric ratio could enhance the impact-resistant capabilities of the structure remarkably. In 2019, experiments and numerical simulation analysis on the hysteretic behavior of 11 buckling-restrained brace specimens (BRBs) with concrete-filled GFRP tubes and

3 BRBs with CFST were conducted by Sun et al. [29], and the results showed that all BRBs exhibited good seismic behavior, and the GFRP tube could be used as an alternative to the traditional outer restraining tube. Experiments on the uniaxial compression behavior of 41 FRP tube-concrete-encased steel (FTCES) columns were carried out by Ren et al. [30], and an analysis-based path-dependent load-strain model was proposed and confirmed. Quasi-static experiments of 13 GFRP-tube-confined recycled concrete columns and GFRP-tube-confined high-strength ordinary concrete columns under cyclic axial compression were studied by Hui et al. [31], and the failure trend of GFRP tubes confined by recycled concrete columns was similar to that of GFRP-tube-confined high-strength ordinary concrete columns, and the axial compression-bearing capacity of the composite columns could be effectively improved by GFRP tubes; finally, the axial load-bearing capacity of GFRP tube concrete columns was derived based on the mechanical equilibrium conditions.

In recent years, composite structures encased with GFRP tubes have also been widely used in civil engineering. An experimental study on axial compressive behavior of concrete-filled circular hollow section stub columns with inner FRP was carried out by Long et al. [32], and the ultimate load-bearing capacity of the composite columns was slightly overpredicted by a simple superposition theory; finally, by introducing a reduction coefficient, a reasonable formula for calculating the ultimate axial compression-bearing capacity was proposed. In 2019, experimental research and numerical analysis of FRP-confined concrete core-encased rebar for RC columns under seismic load were conducted by Wang et al. [33], and by considering the compressive behavior enhancement effect, the minimum FRP tube diameter required for the composite columns was calculated. In 2022, a series of studies on the mechanical properties of rectangular hollow section concrete-filled GFRP tubes (HS-CFGT) were performed by Chen et al. [34] and Yuan et al. [35], and the ultimate bending capacities, load–displacement curves, moment–strain curves and failure modes could be obtained, and the results showed that the flexural behavior highly depended on the material properties of the GFRP tubes.

Thus far, although there have been many kinds of research on the mechanical properties of GFRP-confined concrete columns and special-shaped columns, there are few studies on the mechanical properties of special-shaped composite columns with GFRP core columns. In order to obtain the axial compression performance of this new type of composite column, this paper carried out a numerical analysis for the axial compression performance of 27 special-shaped composite columns with GFRP core columns by ABAQUS finite element software, and the influenced regularity of different parameters on the axial compression performance of this kind of composite column was obtained, and then, the stress mechanism of the special-shaped composite columns was clarified. Finally, by introducing the restraint effect coefficients of GFRP tubes (λ_t) and the stirrups (λ_s), and the reduction coefficient (η), the formula for calculating the axial-bearing capacity of this new type of composite column was proposed by statistical regression, which could lay a foundation for the popularization and application of this kind of column in practical projects.

2. Specimen Design

In order to investigate the mechanical behavior of EGCSSCs subjected to axial load, 27 full-scale EGCSSCs were designed, and the main parameters were the axial compressive strength of core concrete (f_{cc}), axial compressive strength of peripheral concrete (f_{co}), thickness of GFRP tube (t_{grp}), ratio of longitudinal reinforcement (ρ_v), stirrup ratio (ρ_s) and GFRP ratio in the cross-section (α). The specimens were designed and parameters were selected according to the technical specification for concrete structures with specially shaped columns (JGJ149-2017) and reference [13]. The schematic diagram of the EGCSSC is shown in Figure 1. The specific parameters of the EGCSSCs are shown in Table 1. Hot rolled ribbed bar with yield strength of 335 MPa (HRB335) [36] was adopted as longitudinal steel bars with a diameter of 14, 16 and 18 mm, and HRB335 was adopted as stirrups with a diameter of 8 mm, and the protective layer thickness (α_s) was set to 20 mm.

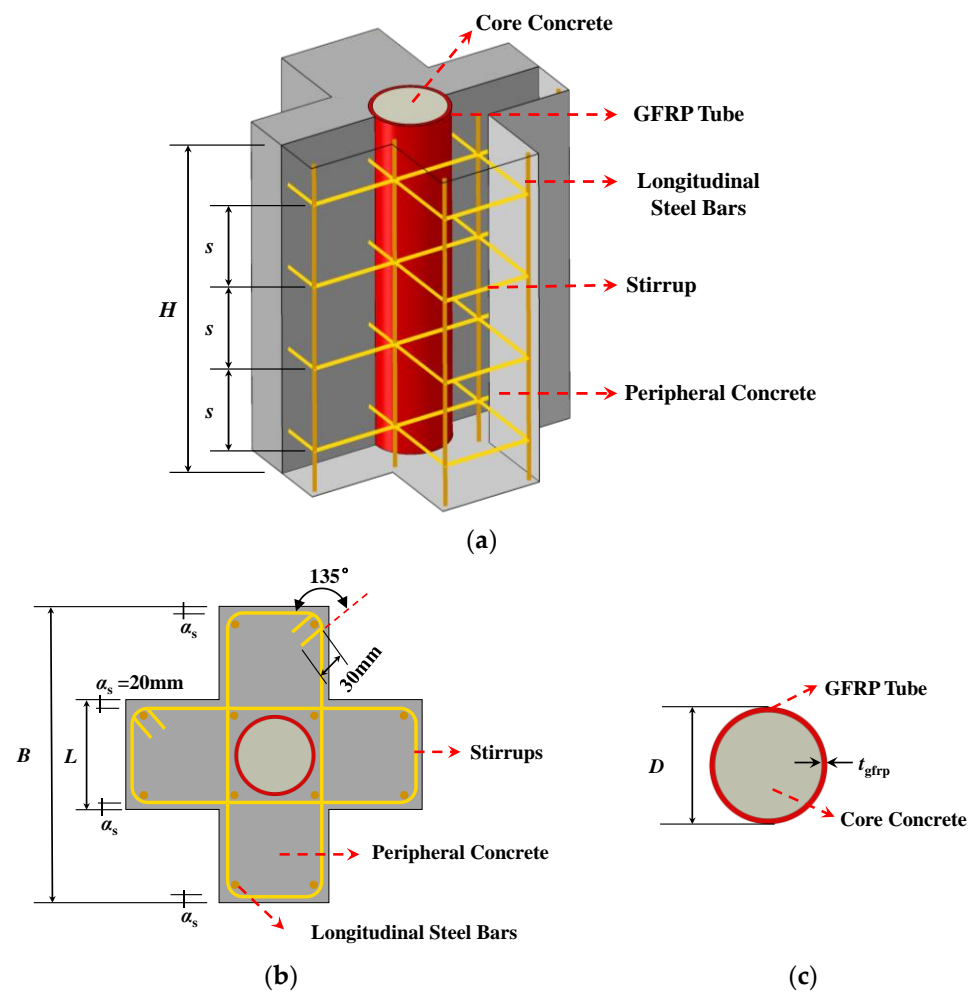


Figure 1. The schematic diagrams of the EGCSSC: (a) the composition of EGCSSC; (b) the cross-section of EGCSSC; (c) the cross-section of the GFRP core column.

Table 1. Specific parameters of 27 EGCSSCs.

Specimen	B/mm	H/mm	L/mm	D/mm	$t_{\text{gfrp}}/\text{mm}$	f_{cc}/MPa	f_{co}/MPa	$\rho_v/\%$	$\rho_s/\%$	$\alpha/-$
SSC-1	800	2400	260	156	3	44.5	26.8	0.9	0.5	0.6
SSC-2	800	2400	260	156	3	44.5	20.1	0.9	0.5	0.6
SSC-3	800	2400	260	156	3	44.5	32.4	0.9	0.5	0.6
SSC-4	800	2400	260	156	3	38.5	26.8	0.9	0.5	0.6
SSC-5	800	2400	260	156	3	50.2	26.8	0.9	0.5	0.6
SSC-6	800	2400	260	104	3	44.5	26.8	0.9	0.5	0.4
SSC-7	800	2400	260	208	3	44.5	26.8	0.9	0.5	0.8
SSC-8	800	2400	260	156	1	44.5	26.8	0.9	0.5	0.6
SSC-9	800	2400	260	156	5	44.5	26.8	0.9	0.5	0.6
SSC-10	800	2400	260	156	3	44.5	26.8	0.5	0.5	0.6
SSC-11	800	2400	260	156	3	44.5	26.8	1.5	0.5	0.6
SSC-12	800	2400	260	156	3	44.5	26.8	0.9	1	0.6
SSC-13	800	2400	260	156	3	44.5	26.8	0.9	1.5	0.6
SSC-14	1000	3000	340	204	3	44.5	20.1	0.9	0.5	0.6
SSC-15	1000	3000	340	204	3	44.5	32.4	0.9	0.5	0.6
SSC-16	1000	3000	340	204	3	44.5	26.8	0.9	0.5	0.6
SSC-17	1000	3000	340	204	3	38.5	26.8	0.9	0.5	0.6

Table 1. Cont.

Specimen	B/mm	H/mm	L/mm	D/mm	$t_{\text{grfp}}/\text{mm}$	f_{cc}/MPa	f_{co}/MPa	$\rho_v/\%$	$\rho_s/\%$	$\alpha/-$
SSC-18	1000	3000	340	204	3	50.2	26.8	0.9	0.5	0.6
SSC-19	1000	3000	340	136	3	44.5	26.8	0.9	0.5	0.4
SSC-20	1000	3000	340	272	3	44.5	26.8	0.9	0.5	0.8
SSC-21	1000	3000	340	204	1	44.5	26.8	0.9	0.5	0.6
SSC-22	1000	3000	340	204	5	44.5	26.8	0.9	0.5	0.6
SSC-23	1000	3000	340	204	3	44.5	26.8	0.5	0.5	0.6
SSC-24	1000	3000	340	204	3	44.5	26.8	1.5	0.5	0.6
SSC-25	1000	3000	340	204	3	44.5	26.8	0.9	1	0.6
SSC-26	1000	3000	340	204	3	44.5	26.8	0.9	1.5	0.6
SSC-27	800	2400	260	0	0	44.5	26.8	0.9	0.5	0

Note: B is the cross-section height of EGCSSCs. H is the height of the EGCSSCs. L is the cross-section width of EGCSSCs. D is the diameter of the GFRP tube. $\rho_v = A_{ss}/A_{co}$; $\rho_s = A_{sv} \cdot l / (A_{co} \cdot s)$. $\alpha = D/L$. $s = 150$ mm. A_{co} is the section area of the EGCSSCs. A_{ss} is the section area of longitudinal steel bars. A_{sv} is the section area of the stirrup. l is the length of the stirrup. s is the spacing of the stirrups.

3. Finite Element Model of EGCSSCs

3.1. Materials Constitutive Model

3.1.1. Steel Bars and Stirrups

Considering the yield strengthening of steel bars, the ideal bilinear model was adopted as the elastic–plastic constitutive model (CM) of the steel bars and stirrups as shown in Figure 2a and Equation (1), where ε_{sy} and f_{sy} are the yield strain and yield strength of steel, respectively, and E_0 is equal to $0.01 E_s$.

$$\sigma_i = \begin{cases} E_s \times \varepsilon & (\varepsilon \leq \varepsilon_y) \\ f_{sy} + E_0 \times (\varepsilon - \varepsilon_{sy}) & (\varepsilon_y < \varepsilon) \end{cases} \quad (1)$$

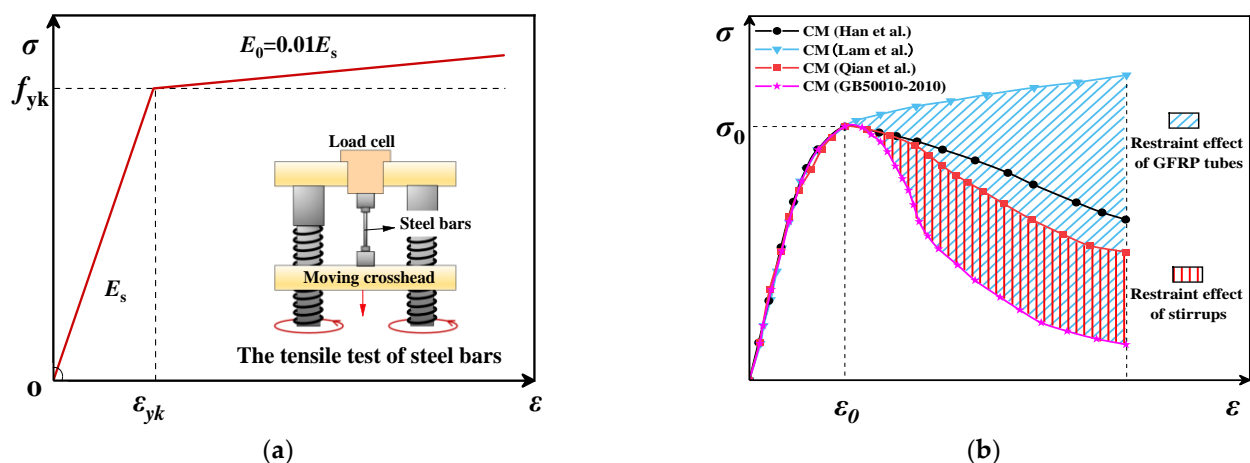


Figure 2. Constitutive models for materials: (a) steel bars and stirrups; (b) concrete [15,27,37,38].

3.1.2. Concrete

By comparing the CMs of concrete proposed by Qian et al. [37], Lam et al. [27], Han et al. [15], and the Code for Design of Concrete Structure (GB50010-2010) [38], the CMs of confined concrete proposed by Qian and Lam were selected as the CMs for periphery concrete and core concrete, respectively. The comparisons of CMs for concrete are shown in Figure 2b. The proposed stress–strain models for peripheral and core concrete under axial compression are shown in Equations (2)–(4).

The stress–strain relationship of peripheral concrete under axial compression:

$$y = \begin{cases} ax + (3 - 2a)x^2 + (a - 2)x^3 & (0 \leq x \leq 1) \\ \frac{x}{(1 - 0.87\lambda_v^{0.2})T[x-1]^2 + x} & (1 < x) \end{cases} \quad (2)$$

where $x = \varepsilon/\varepsilon_0$, $y = \sigma/\sigma_0$, $\sigma_0 = (1 + 1.79\lambda_v)f_{co1}$, $\varepsilon_0 = (1 + 3.50\lambda_v)\varepsilon_{co1}$, $a = 2.1 - 0.001f_{cu}$, $T = 0.132f_{cu} - 0.785 - 0.905$. σ_0 is axial compression strength of concrete. ε_0 is peak strain corresponding to σ_0 . λ_v is stirrup characteristic value. f_{co1} is axial compressive strength of plain concrete. ε_{co1} is peak strain corresponding to f_{co1} . f_{cu} is the concrete cube compressive strength. T is the descending parameter.

The stress–strain relationship of core concrete under axial compression:

$$\sigma'_c = \begin{cases} E_c\varepsilon_c - \frac{(E_c - E'_2)^2}{4f'_{co}}\varepsilon_c^2 & (0 \leq \varepsilon_c \leq \varepsilon_t) \\ f'_{co} + E'_2\varepsilon_c & (\varepsilon_t < \varepsilon_c < \varepsilon'_{cc}) \end{cases} \quad (3)$$

where $\varepsilon_t = 2f'_{co}/(E_c - E'_2)$, $E'_2 = (f'_{cc} - f'_{co})/\varepsilon'_{cc}$.

E_c is the elastic modulus of concrete. E'_2 is the initial elastic modulus of concrete. ε_t is the strain corresponding to the intersection of the curves. f'_{cc} and f'_{co} are the compressive strengths of the confined and the unconfined concrete, respectively. ε'_{cc} is the ultimate strain.

The stress–strain relationship of concrete under axial tension:

$$y = \begin{cases} 1.2x - 0.2x^6 & (0 < x \leq 1) \\ \frac{x}{0.31\sigma_p^2[x-1]^{1.7} + x} & (1 < x) \end{cases} \quad (4)$$

where $x = \varepsilon_c/\varepsilon_p$, $y = \sigma_c/\sigma_p$, $\sigma_p = 0.26(1.25f_c)2/3$, $\varepsilon_p = 43.1\sigma_p$, σ_c is tensile stress, ε_c is concrete strain, σ_p is the peak tensile stress, and ε_p is the peak tensile strain.

3.1.3. GFRP Tube

GFRP tube is a kind of fiber-reinforced composite material with anisotropic mechanical properties. Therefore the single-layer plate model and the Hashin failure criterion in ABAQUS were adopted as the CM of the GFRP tube. The mechanical behavior of the GFRP material is shown in Table 2.

Table 2. Mechanical behavior of the GFRP material.

E_1 /MPa	E_2 /MPa	ν_{12} /-	G_{12} /MPa	X_T /MPa	X_c /MPa	Y_T /MPa	Y_c /MPa	θ /°	t_r /mm
52,000	8000	0.32	3000	584	203	43	187	±80	0.5

Note: E_1 and E_2 represent the elastic modulus of GFRP in the tangential and normal directions, respectively. ν_{12} is the Poisson's ratio. G_{12} represents the shear modulus. X_T and X_c are the longitudinal tensile strength and compressive strength, respectively. Y_T and Y_c are the transverse tensile strength and compressive strength. θ is the relative laying angle adjacent layers of GFRP. t_r is the relative thickness of adjacent layers of GFRP.

3.1.4. Concrete Plastic Damage Model

In this paper, the concrete plastic damage model was adopted to simulate the concrete element in the column. The definition of concrete plastic damage is shown in Table 3.

Table 3. The parameters of concrete plastic damage model.

Dilation Angle/°	Eccentric Ratio/-	f_{bo}/f_{co} /-	K' /-	Viscosity Parameter/-
30	0.1	1.16	0.667	0.0005

Note: K' is the second stress invariant ratio. f_{bo}/f_{co} is the Bi-axial to uni-axial strength ratio.

3.2. Establishment of Refined Finite Element Model

3.2.1. Element Type and Meshing

The finite element models of EGCSSCs were established by ABAQUS in this paper. Steel bars and stirrups were established by T3D2, core and peripheral concrete were established by C3D8R, and GFRP tube was established by S4R. To simplify the model and improve the calculation accuracy, 20 mm was set as the global mesh size of the finite element model [39,40].

3.2.2. Interaction and Boundary Conditions

During the process of finite element modeling, it was assumed that there was no bond slip between GFRP tube and core and peripheral concrete, which are connected by binding. The hard contact was adopted between the GFRP tube and core and peripheral concrete in the normal direction. Considering the relative slip, the friction contact was adopted between the GFRP tube and core and peripheral concrete in the tangential direction, and the friction coefficient was set to 0.5 [39]. Two reference points RP_1 and RP_2 were set at a distance of 10 mm away from the center between two ends of EGCSSCs. RP_1 was limited by displacement and rotation ($U_1 = U_2 = 0$, $UR_1 = UR_2 = 0$ rad/s), and RP_2 was completely fixed, restricting the displacement in X, Y, and Z directions ($U_1 = U_2 = U_3 = 0$) and the rotation in three directions ($UR_1 = UR_2 = UR_3 = 0$ rad/s). The finite element model of EGCSSCs is shown in Figure 3.

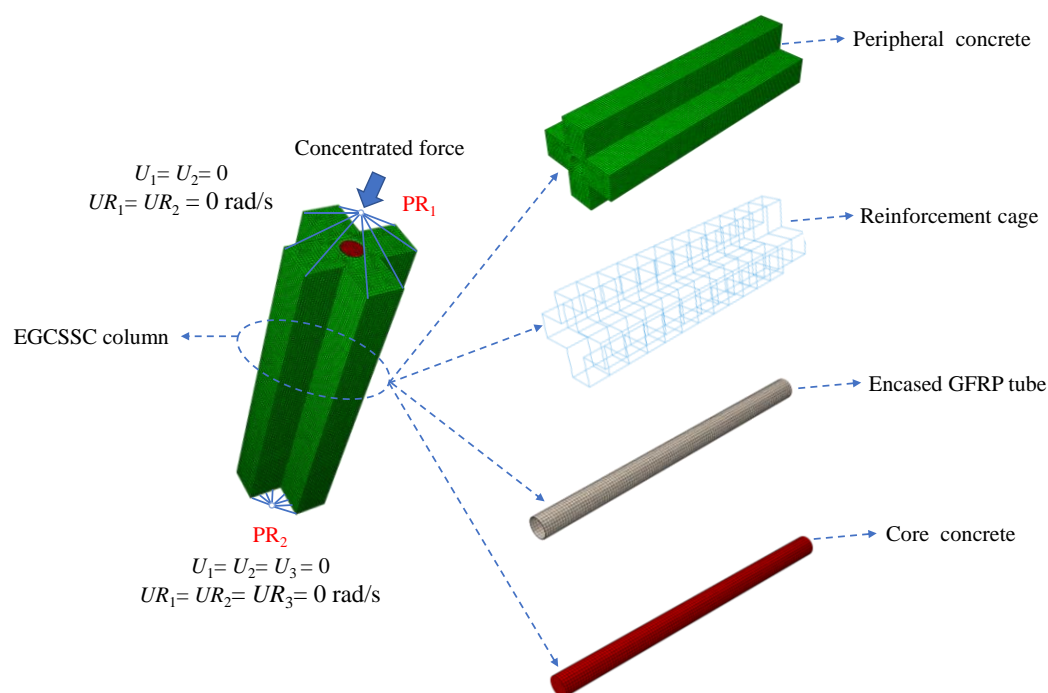


Figure 3. The finite element model of EGCSSCs.

4. Experimental Validation of Finite Element Models

Eight rectangular reinforced concrete columns under axial compression designed by Che et al. [41] and Radnic et al. [42] and eight middle-long columns of high-strength concrete-filled square steel tube with inner CFRP circular tube under axial compression designed by Li et al. [43,44] were selected to verify the rationality of the above modeling method. The specific data of sixteen specimens are shown in Table 4.

By finite element simulation, the load–strain (N – ϵ) curves of the above composite columns could be obtained, which are shown in Figure 4. It can be seen that the N – ϵ curves were in good agreement. The comparative results of the ultimate bearing capacity obtained by simulations (N_s) and experiments (N_t) are shown in Table 4 and Figure 5, and the

maximum error ($Error_{MAX}$) between N_s and N_t was 5.33%; therefore, the rationality of the FEM was verified, and the ultimate bearing capacity of the specimen could be predicted accurately by the finite element model.

Table 4. The comparison of the bearing capacity under axial compression between the simulation and experiment for sixteen specimens.

Specimens		$H \times b_{cor} \times d_s \times s (\times s_2)$ or $B_1 \times D_c \times H \times t_c \times t_s / (mm)$	f_y / MPa	f_c / MPa	N_s / kN	N_t / kN	$\frac{ N_s - N_t }{N_s} / \%$
Che et al. [41]	A-1	$354 \times 95 \times 3.5 \times 27 \times 13.5$	383	42.31	387.89	384.90	0.77
	B-1	$630 \times 176 \times 6 \times 50 \times 25$	532	42.31	1030.00	978.20	5.03
	C-1	$780 \times 218 \times 8 \times 62.5 \times 31.3$	644	44.43	1985.27	1997.10	0.60
	D-1	$1140 \times 326 \times 12 \times 92.5 \times 43.6$	382	49.73	4408.98	4298.20	2.51
Radnic et al. [42]	RC-1	$600 \times 90 \times 8 \times 50$	560	24.9	386.61	387.36	0.19
	RC-2	$600 \times 90 \times 8 \times 50$	560	35.2	519.33	532.6	2.56
	RC-3	$600 \times 90 \times 8 \times 50$	560	45.1	634.89	657.11	3.50
	RC-4	$600 \times 90 \times 4 \times 75$	500	45.1	554.75	538.59	2.91
Li et al. [43]	CFSSC-3	$200 \times 150 \times 800 \times 0.334 \times 5$	320	90	4421.49	4560.00	3.13
	CFSSC-6	$200 \times 150 \times 1200 \times 0.334 \times 5$	320	90	4535.05	4374.00	3.55
	CFSSC-8	$200 \times 150 \times 1600 \times 0.334 \times 5$	320	90	4267.99	4280.00	0.28
	CFSSC-10	$200 \times 150 \times 2000 \times 0.334 \times 5$	320	90	4445.83	4209.00	5.33
Li et al. [44]	CFSSC-2-1	$200 \times 150 \times 2600 \times 0.334 \times 5$	320	92	3926.6	3986	1.51
	CFSSC-2-2	$200 \times 150 \times 2800 \times 0.334 \times 5$	320	92	4068.13	3910	3.89
	CFSSC-2-3	$200 \times 150 \times 3000 \times 0.334 \times 5$	320	92	3879.7	3760	3.09
	CFSSC-2-4	$200 \times 150 \times 3200 \times 0.334 \times 5$	320	92	3331.13	3490	4.77

Note: B_1 is the width of the section. D_c is the diameter of the CFRP tube. t_c is the thickness of the CFRP tube. t_s is the thickness of the steel tube. b_{cor} is the length of the core concrete. d_s is the diameter of the stirrup. s_1 is the stirrup spacing in the densification zone. f_y is the yield strength of the rectangular steel tube or the steel bar. f_c is the compressive strength of the concrete.

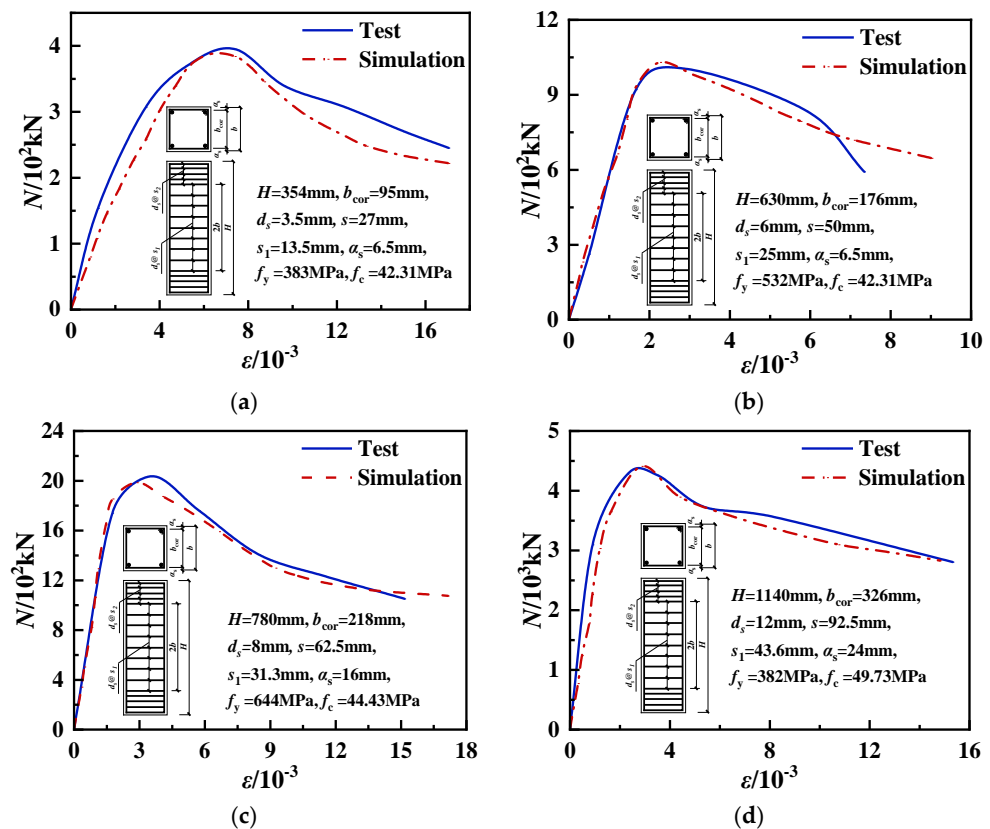


Figure 4. Cont.

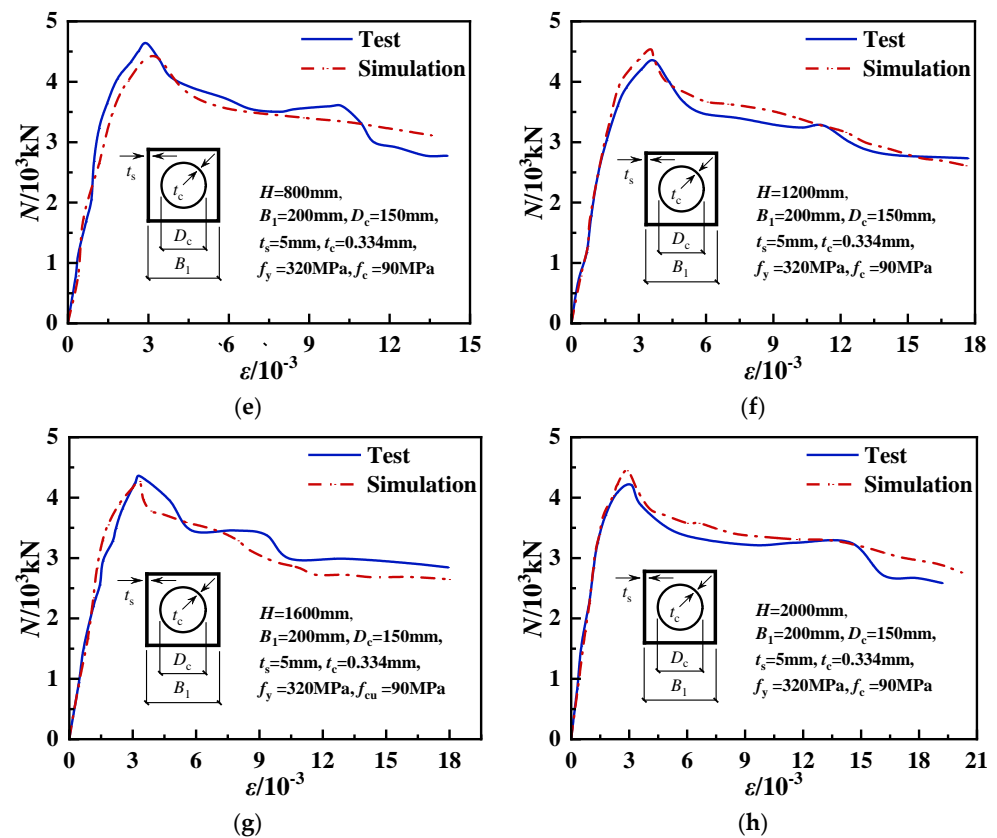


Figure 4. Comparison of N - ε curves between simulation and test: (a) A-1. (b) B-1. (c) C-1. (d) D-1. (e) CFSSC-3. (f) CFSSC-6. (g) CFSSC-8. (h) CFSSC-10.

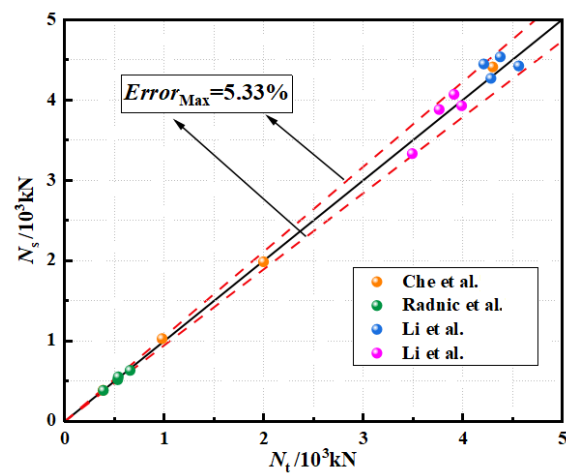


Figure 5. Comparison of N_s and N_t for sixteen specimens [41–44].

5. Parameter Analysis of EGCSSCs

The initial stiffness (K) and ductility index (μ) of EGCSSCs were calculated by the equivalent elastoplastic energy method [45,46]. The calculation formula of μ is shown in Equation (5) and Figure 6. The results of K and μ of 27 specimens are shown in Figures 7–19 and Table 5. The N - ε curves of the 27 EGCSSCs under axial load are shown in Figures 7–19. The main parameters are: (1) Axial compressive strength of core concrete (f_{cc}) (from 38.5 to 50.2 MPa). (2) Axial compressive strength of peripheral concrete (f_{co}) (from 20.1 to 32.4 MPa). (3) Thickness of GFRP tube (t_{gfrp}) (from 1 to 5 mm). (4) Ratio of longitudinal reinforcement (ρ_v) (from 0.5% to 1.5%). (5) Stirrup ratio (ρ_s) (from 0.5% to 1.5%). (6) GFRP ratio of section (α) (from 0 to 0.8).

$$\mu = \frac{\Delta_u}{\Delta_y} \tag{5}$$

where Δ_u is the ultimate displacement of EGCSSCs. Δ_y is the yielding displacement of EGCSSCs.

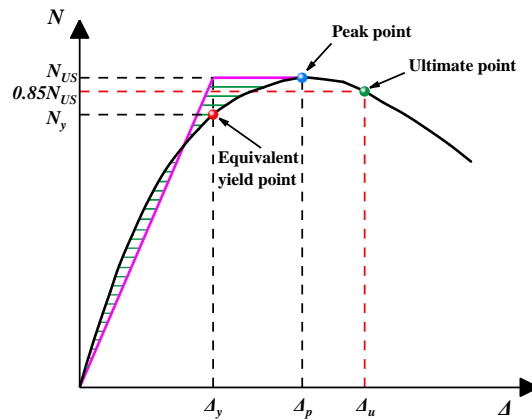


Figure 6. The equivalent elastoplastic energy method.

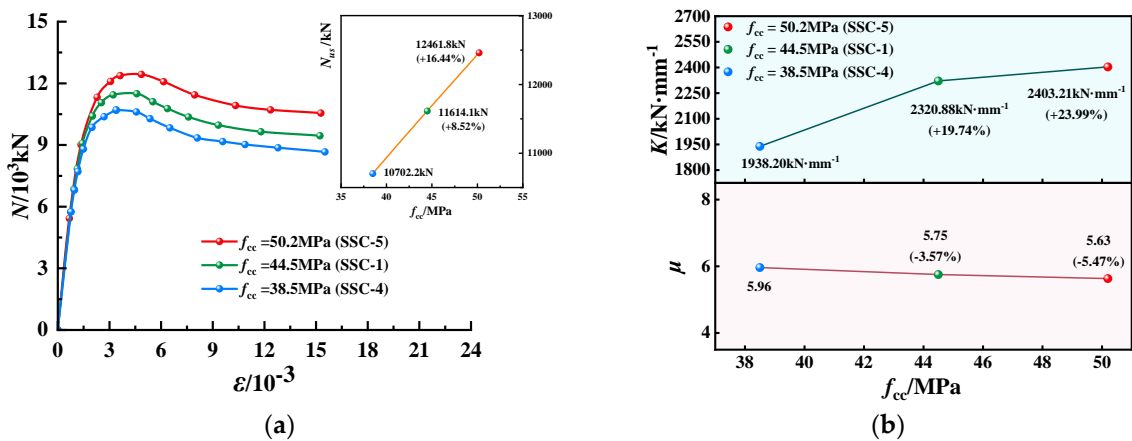


Figure 7. N - ϵ curves, K and μ of EGCSSCs with different f_{cc} : (a) N - ϵ curves of specimens with cross-section height of 800 mm. (b) K and μ of specimens with cross-section height of 800 mm.

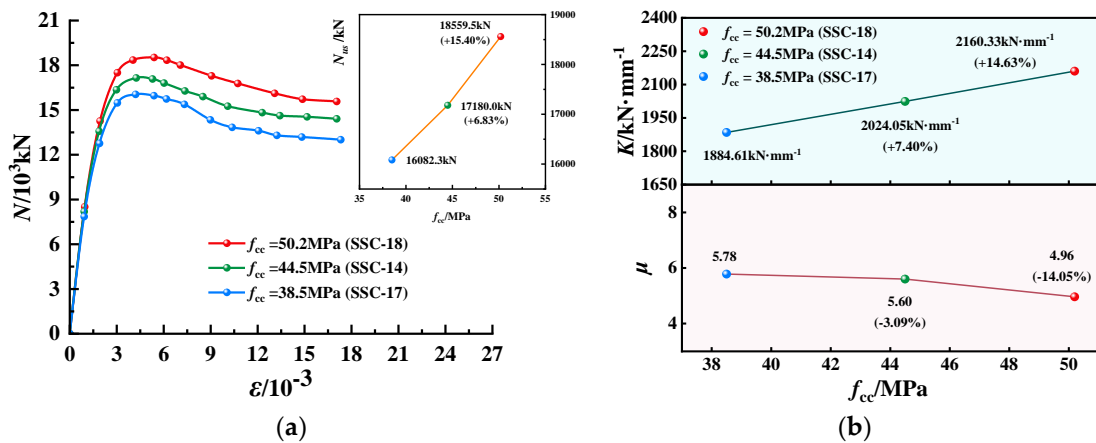


Figure 8. N - ϵ curves, K and μ of EGCSSCs with different f_{cc} : (a) N - ϵ curves of specimens with cross-section height of 1000 mm. (b) K and μ of specimens with cross-section height of 1000 mm.

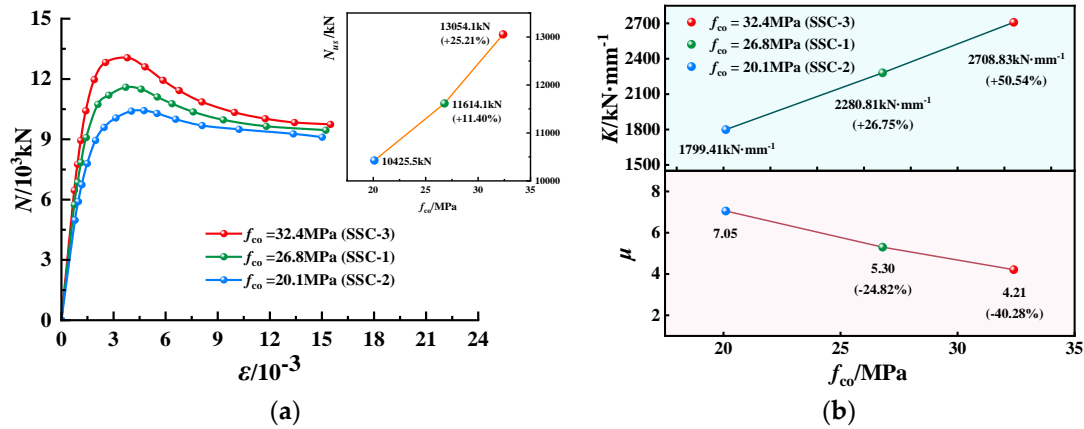


Figure 9. N - ϵ curves, K and μ of EGCSSCs with different f_{co} : (a) N - ϵ curves of specimens with cross-section height of 800 mm. (b) K and μ of specimens with cross-section height of 800 mm.

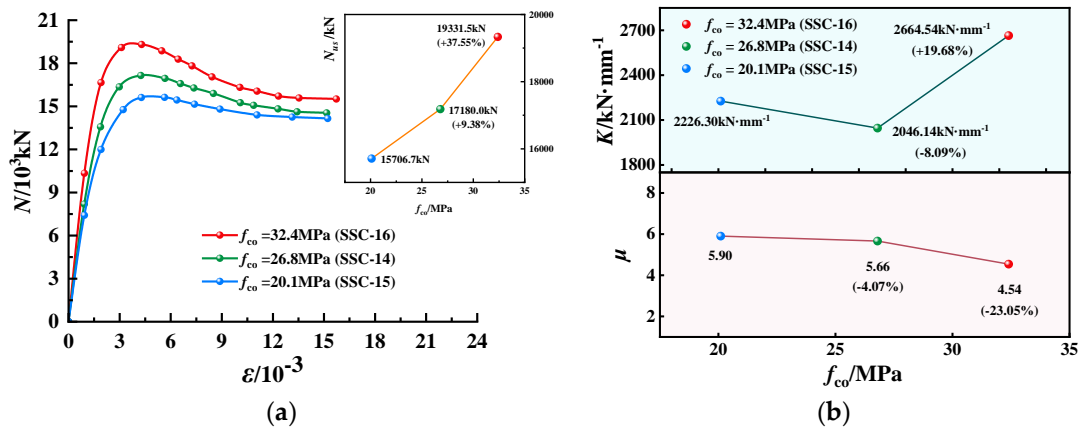


Figure 10. N - ϵ curves, K and μ of EGCSSCs with different f_{co} : (a) N - ϵ curves of specimens with cross-section height of 1000 mm. (b) K and μ of specimens with cross-section height of 1000 mm.

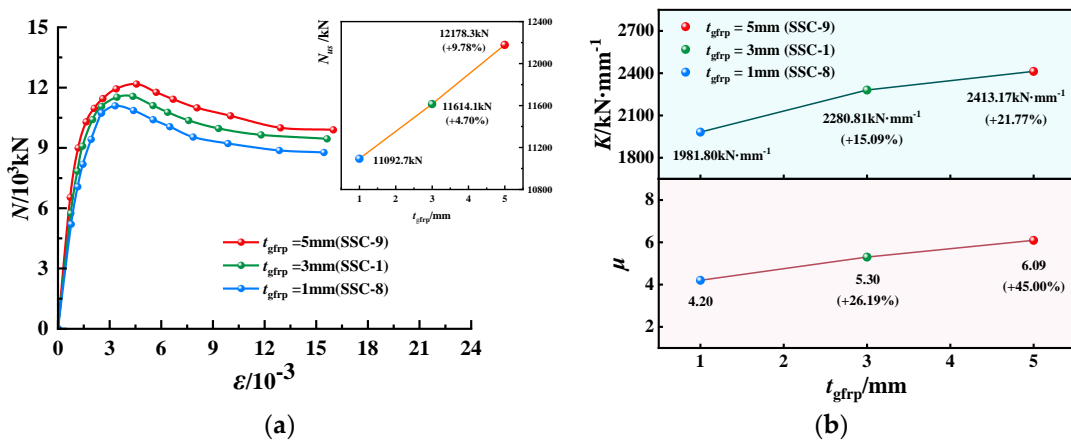


Figure 11. N - ϵ curves, K and μ of EGCSSCs with different t_{grfp} : (a) N - ϵ curves of specimens with cross-section height of 800 mm. (b) K and μ of specimens with cross-section height of 800 mm.

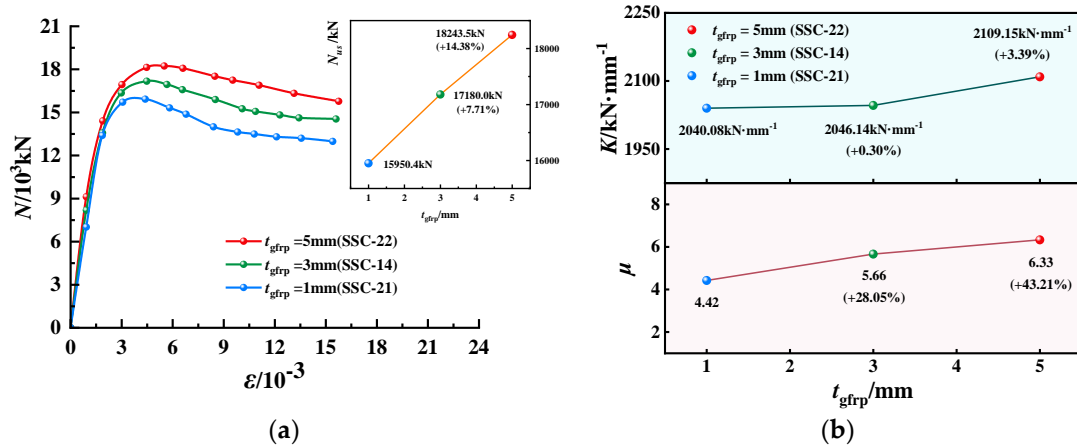


Figure 12. N - ϵ curves, K and μ of EGCSSCs with different t_{gfrp} : (a) N - ϵ curves of specimens with cross-section height of 1000 mm. (b) K and μ of specimens with cross-section height of 1000 mm.

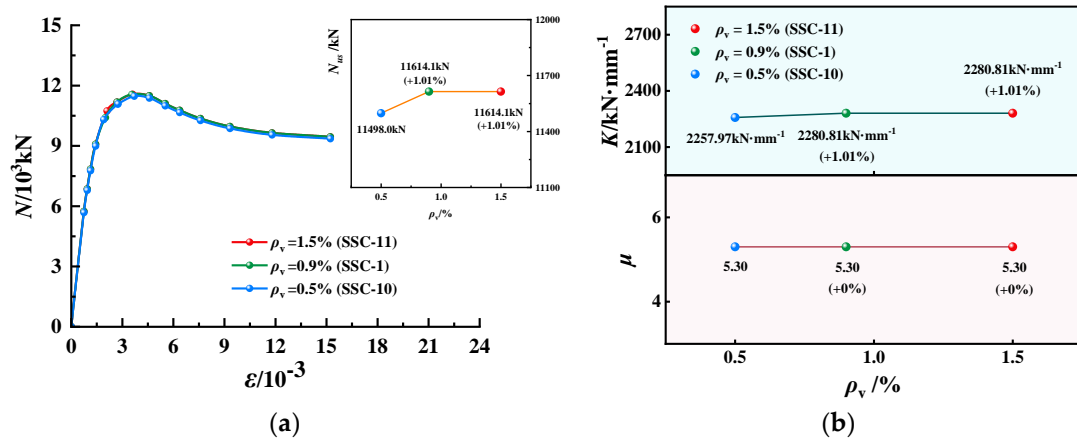


Figure 13. N - ϵ curves, K and μ of EGCSSCs with different ρ_v : (a) N - ϵ curves of specimens with cross-section height of 800 mm. (b) K and μ of specimens with cross-section height of 800 mm.

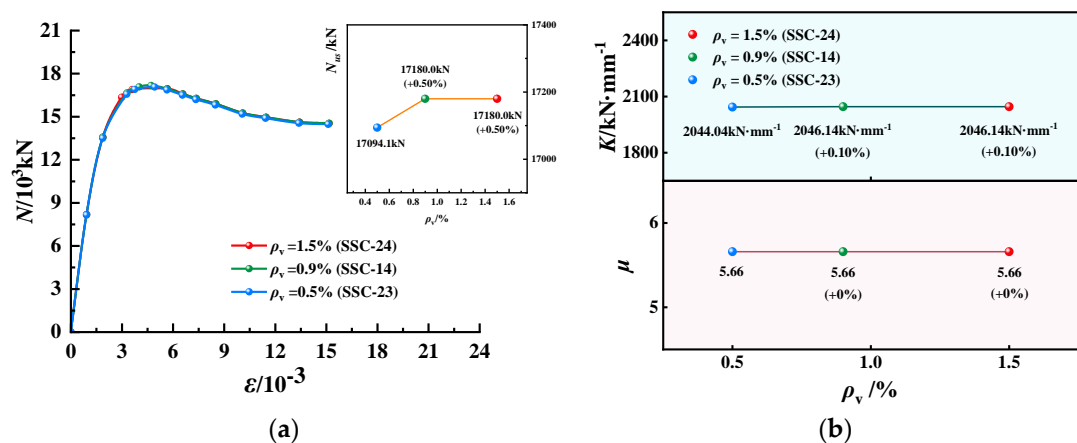


Figure 14. N - ϵ curves, K and μ of EGCSSCs with different ρ_v : (a) N - ϵ curves of specimens with cross-section height of 1000 mm. (b) K and μ of specimens with cross-section height of 1000 mm.

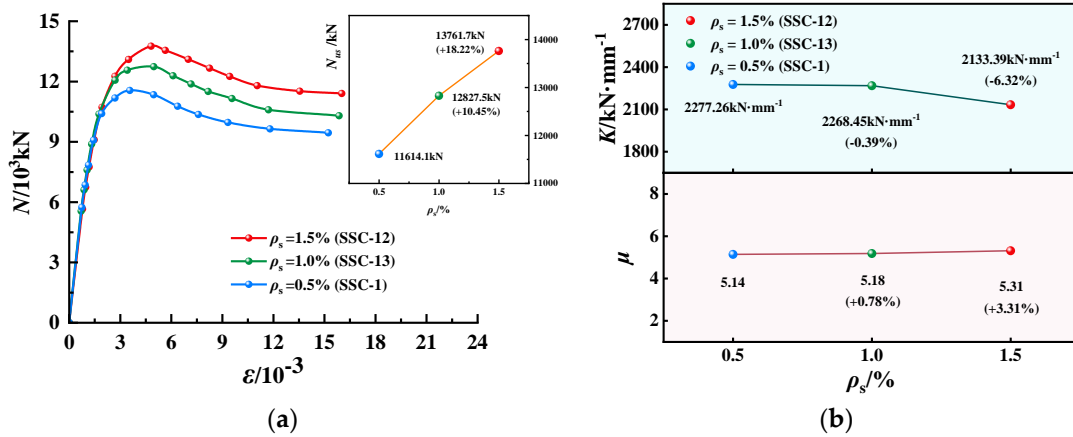


Figure 15. $N-\epsilon$ curves, K and μ of EGCSSCs with different ρ_s : (a) $N-\epsilon$ curves of specimens with cross-section height of 800 mm. (b) K and μ of specimens with cross-section height of 800 mm.

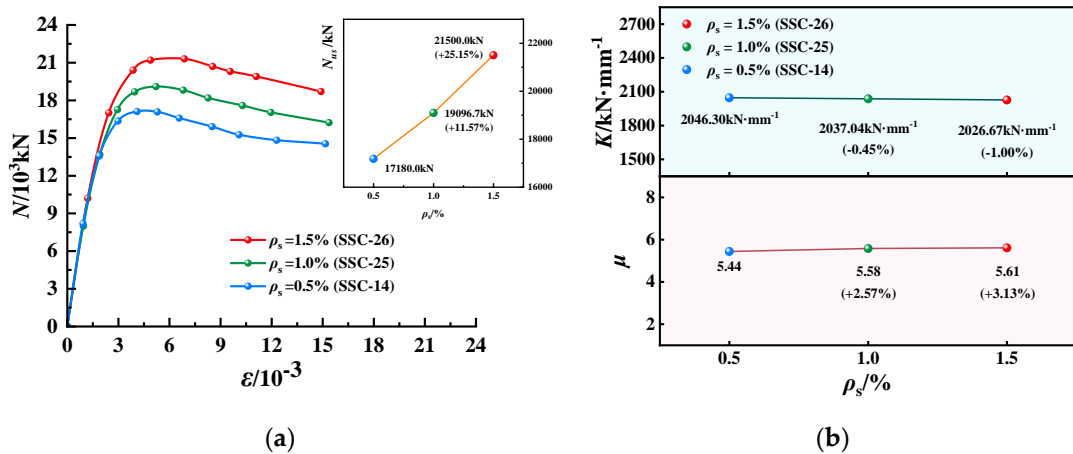


Figure 16. $N-\epsilon$ curves, K and μ of EGCSSCs with different ρ_s : (a) $N-\epsilon$ curves of specimens with cross-section height of 1000 mm. (b) K and μ of specimens with cross-section height of 1000 mm.

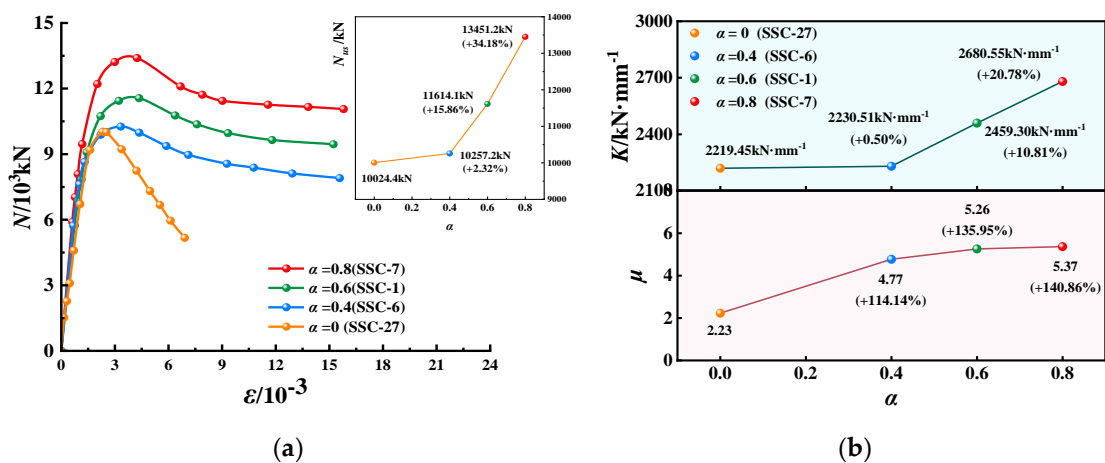


Figure 17. $N-\epsilon$ curves, K and μ of EGCSSCs with different α : (a) $N-\epsilon$ curves of specimens with cross-section height of 800 mm. (b) K and μ of specimens with cross-section height of 800 mm.

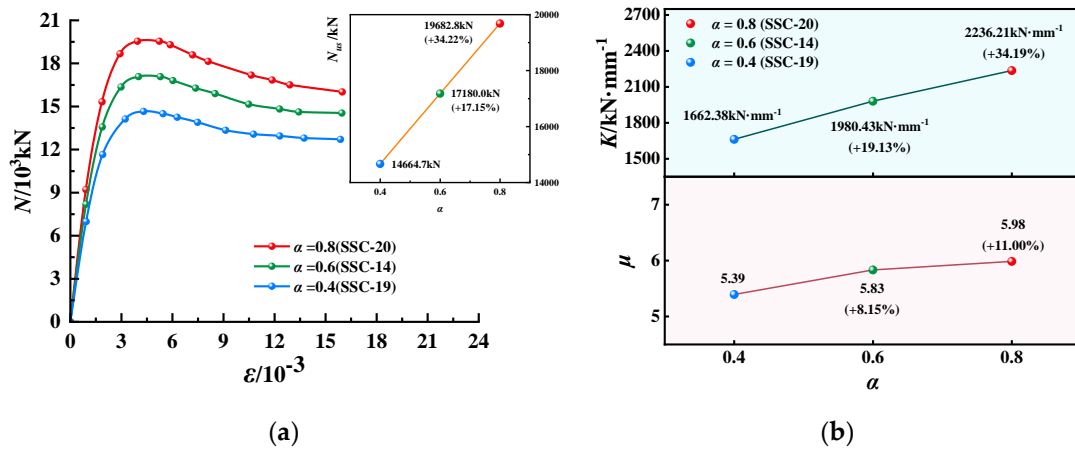


Figure 18. N - ϵ curves, K and μ of EGCSSCs with different α : (a) N - ϵ curves of specimens with cross-section height of 1000 mm. (b) K and μ of specimens with cross-section height of 1000 mm.

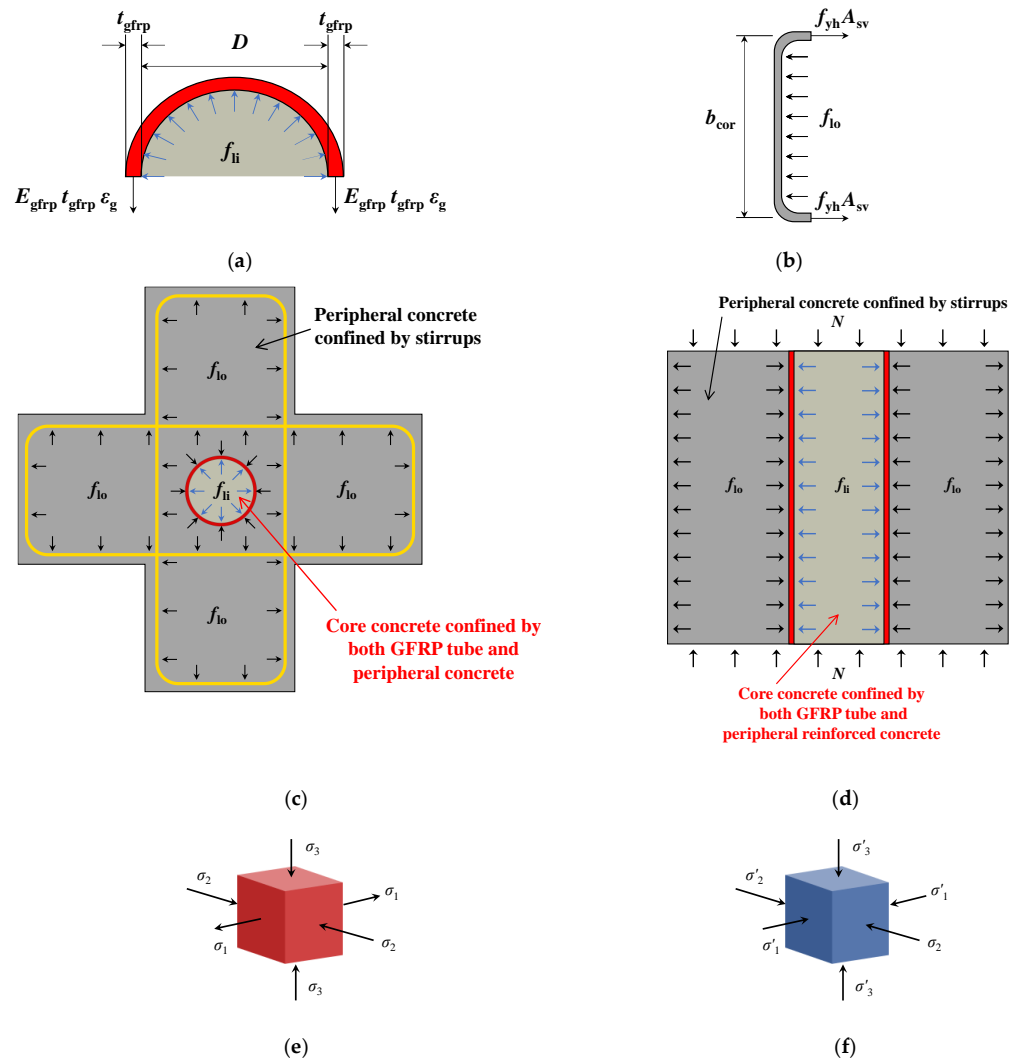


Figure 19. The stress states of different parts: (a) Concrete constrained by GFRP tube. (b) Concrete constrained by stirrup. (c) The cross-section of EGCSSCs. (d) The profile of EGCSSCs. (e) The element of GFRP tube. (f) The element of core and peripheral concrete.

Table 5. K and μ of EGCSSCs with different parameters.

Specimens		B/mm	$K/kN \cdot mm^{-1}$	Δ_y/mm	Δ_u/mm	$\mu/-$	
SSC-4	f_{cc}/MPa	38.5	800	1938.20	5.08	30.28	5.96
SSC-1		44.5	800	2320.88	4.36	25.06	5.75
SSC-5		50.2	800	2403.21	4.16	23.44	5.63
SSC-17		38.5	1000	1884.61	7.96	45.97	5.78
SSC-14		44.5	1000	2024.05	7.41	41.47	5.60
SSC-18		50.2	1000	2160.33	6.89	34.2	4.96
SSC-2	f_{co}/MPa	20.1	800	1799.41	5.11	36.05	7.05
SSC-1		26.8	800	2280.81	4.54	24.07	5.30
SSC-3		32.4	800	2708.83	4.30	18.11	4.21
SSC-15		20.1	1000	226.30	6.19	36.53	5.90
SSC-14		26.8	1000	2046.14	7.33	41.47	5.66
SSC-16		32.4	1000	2664.54	6.43	29.20	4.54
SSC-8	t_{gfrp}/mm	1	800	1981.80	4.87	20.45	4.20
SSC-1		3	800	2280.81	4.54	24.07	5.30
SSC-9		5	800	2413.17	4.41	26.85	6.09
SSC-21		1	1000	2040.08	7.02	41.47	4.42
SSC-14		3	1000	2046.14	7.33	47.28	5.66
SSC-22		5	1000	2109.15	7.47	41.34	6.33
SSC-10	$\rho_v/\%$	0.5	800	2257.97	4.54	24.07	5.30
SSC-1		0.9	800	2280.81	4.54	24.07	5.30
SSC-11		1.5	800	2280.81	4.54	24.07	5.30
SSC-23		0.5	1000	2044.04	7.30	41.47	5.66
SSC-14		0.9	1000	2046.14	7.33	41.47	5.66
SSC-24		1.5	1000	2046.14	7.33	41.47	5.66
SSC-1	$\rho_s/\%$	0.5	800	2277.26	4.68	24.07	5.14
SSC-13		1.0	800	2268.45	4.87	25.26	5.18
SSC-12		1.5	800	2133.39	5.40	28.68	5.31
SSC-14		0.5	1000	2046.30	7.62	41.47	5.44
SSC-25		1.0	1000	2037.04	8.25	46.08	5.58
SSC-26		1.5	1000	2026.67	8.55	48.00	5.61
SSC-27	$\alpha/-$	0.0	800	2219.45	4.22	9.40	2.23
SSC-6		0.4	800	2230.51	4.65	22.18	4.77
SSC-1		0.6	800	2459.30	4.38	23.02	5.26
SSC-7		0.8	800	2680.55	4.41	23.66	5.37
SSC-19		0.4	1000	1662.38	7.86	42.38	5.39
SSC-14		0.6	1000	1980.43	7.35	42.86	5.83
SSC-20	0.8	1000	2236.21	7.23	43.27	5.98	

5.1. Axial Compressive Strength of Core Concrete (f_{cc})

N - ε curves, K and μ of EGCSSCs with different f_{cc} are shown in Figures 7 and 8. As seen in Figure 7, when the values of f_{cc} are given from 38.5 to 44.5 and 50.2 MPa, the ultimate axial-bearing capacity (N_{us}) of specimens with the cross-section height of 800 mm could be increased from 10702.2 to 11614.1 and 12461.8 kN, respectively, which increased by 8.52% and 16.44%. K could be increased from 1938.20 to 2320.88 and 2403.21 $kN \cdot mm^{-1}$, respectively, which increased by 19.74% and 23.99%. However, μ could be decreased from 5.96 to 5.75 and 5.63, respectively, which decreased by 3.57% and 5.47%. As can be seen in Figure 8, when the values of f_{cc} are given from 38.5 to 44.5 and 50.2 MPa, N_{us} of specimens with the cross-section height of 1000 mm could be increased from 16082.3 to 171180.0 and 18,559.5 kN, respectively, which increased by 6.83% and 15.40%. K could be increased from 1884.6 to 2024.05 and 2160.33 $kN \cdot mm^{-1}$, respectively, which increased by 7.40% and 14.63%. However, μ could be decreased from 5.78 to 5.60 and 4.96, respectively, which decreased by 3.09% and 14.05%. It was summarized that with the increase in f_{cc} , the N_{us} and K gradually

increased, while μ gradually decreased. Therefore, f_{cc} was the important parameter to the ultimate axial compression-bearing capacity of EGCSSCs.

5.2. Axial Compressive Strength of Peripheral Concrete (f_{co})

N - ε curves, K and μ of EGCSSCs with different f_{co} are shown in Figures 9 and 10. As seen in Figure 9, when the values of f_{co} are given from 20.1 to 26.8 and 32.4 MPa, N_{us} of specimens with the cross-section height of 800 mm could be increased from 10,425.5 to 11,614.1 and 13,054.1 kN, respectively, which increased by 11.40% and 25.21%. K could be increased from 1799.41 to 2280.81 and 2780.83 kN·mm⁻¹, respectively, which increased by 26.75% and 50.54%. However, μ could be decreased from 7.05 to 5.30 and 4.21, respectively, which decreased by 24.82% and 40.28%. It can be seen in Figure 10, when the values of f_{co} are given from 20.1 to 26.8 and 32.4 MPa, N_{us} of specimens with the cross-section height of 1000 mm could be increased from 15,706.7 to 17,180.0 and 19,331.5 kN, respectively, which increased by 9.38% and 37.55%. K could be decreased from 2226.30 to 2046.14 kN·mm⁻¹ firstly, and then increased to 2664.54 kN·mm⁻¹. μ could be decreased from 5.90 to 5.66 and 4.54, respectively, which decreased by 4.07% and 23.05%. It was summarized that with the increase in f_{co} , the N_{us} and K gradually increased, while the ductility of the EGCSSCs decreased, and the parameter f_{co} had a great influence on the N_{us} , K and μ .

5.3. The Thickness of GFRP Tube (t_{gfrp})

N - ε curves, K and μ of EGCSSCs with different t_{gfrp} are shown in Figures 11 and 12. As seen in Figure 11, when the values of t_{gfrp} are given from 1 to 3 and 5 mm, N_{us} of specimens with the cross-section height of 800 mm could be increased from 11,092.7 to 11,614.1 and 12,178.3 kN, respectively, which increased by 4.70% and 9.78%. K could be increased from 1981.80 to 2280.81 and 2413.14 kN·mm⁻¹, respectively, which increased by 15.09% and 21.77%. μ could be increased from 4.20 to 5.30 and 6.09, respectively, which increased by 26.19% and 45.00%. It can be seen in Figure 12, when the values of t_{gfrp} are given from 1 to 3 and 5 mm, N_{us} of specimens with the cross-section height of 1000 mm could be increased from 15,950.4 to 17,180.0 and 18,243.5 kN, respectively, which increased by 7.71% and 14.38%. K could be increased from 2040.08 to 2046.14 and 2109.15 kN·mm⁻¹, respectively, which increased by 0.30% and 3.39%. μ could be increased from 4.42 to 5.56 and 6.33, respectively, which increased by 28.05% and 43.21%. It was summarized that the N_{us} , K and μ of the specimens gradually increased with the increase in t_{gfrp} , and the specimens all showed good load-holding capacity and excellent deformation ability.

5.4. The Ratio of Longitudinal Reinforcement (ρ_v)

N - ε curves, K and μ of EGCSSCs with different ρ_v are shown in Figures 13 and 14. As seen in Figure 13, when the values of ρ_v are given from 0.5% to 0.9% and 1.5%, N_{us} of specimens with the cross-section height of 800 mm could be increased from 114,985.0 to 11,614.1 kN firstly, and then N_{us} kept unchanged. K could be increased from 2257.97 to 2280.81 kN·mm⁻¹ firstly, and then K kept unchanged. μ was 5.30 and kept unchanged. It can be seen in Figure 14, when the values of ρ_v are given from 0.5% to 0.9% and 1.5%, N_{us} of specimens with the cross-section height of 1000 mm could be increased from 1709.4 to 17,180.0 kN firstly, and then kept unchanged. K could be increased from 2044.04 to 2046.14 kN·mm⁻¹ firstly, and then K kept unchanged. μ was 5.66 and kept unchanged. It was summarized that the change in ρ_v had little effect on the axial compression performance of the EGCSSCs.

5.5. The Stirrup Ratio (ρ_s)

N - ε curves, K and μ of EGCSSCs with different ρ_s are shown in Figures 15 and 16. As seen in Figure 15, when the values of ρ_s are given from 0.5% to 1% and 1.5%, N_{us} of specimens with the cross-section height of 800 mm could be increased from 11,614.1 to 12,827.5 and 13,761.7 kN, respectively, which increased by 10.45% and 18.22%. K could be decreased from 2277.26 to 2268.45 and 2133.39 kN·mm⁻¹, respectively, which decreased

by 0.39% and 6.32%. μ could be increased from 5.14 to 5.18 and 5.31, respectively, which increased by 0.78% and 3.31%. It can be seen in Figure 16, when the values of ρ_s are given from 0.5% to 1% and 1.5%, N_{us} of specimens with the cross-section height of 1000 mm could be increased from 17,180.0 to 19,096.7 and 21,500.0 kN, respectively, which increased by 11.57% and 25.15%. K could be decreased from 2046.30 to 2037.04 and 2026.67 kN·mm⁻¹, respectively, which decreased by 0.45% and 1.00%. μ could be increased from 5.44 to 5.58 and 5.61, respectively, which increased by 2.57% and 3.13%. It was summarized that the N_{us} and μ of the specimens gradually increased with the increase in ρ_s . However, K decreased slowly with the increase in ρ_s .

5.6. The GFRP Ratio in the Cross-Section (α)

N - ϵ curves, K and μ of EGCSSCs with different α are shown in Figures 17 and 18. As seen in Figure 17, when the values of α are given from 0 to 0.4, 0.6 and 0.8, N_{us} of specimens with the cross-section height of 800 mm could be increased from 10,024.4 to 110,257.2, 1161.4 and 13,451.2 kN, respectively, which increased by 2.32%, 15.86% and 34.18%. K could be increased from 2219.45 to 2230.51, 2459.30 and 2680.55 kN·mm⁻¹, respectively, which increased by 0.50%, 10.81% and 20.78%. μ could be increased from 2.23 to 4.77, 5.26 and 5.37, respectively, which increased by 114.14%, 135.95% and 140.86%. It can be seen in Figure 18, when the values of α are given from 0.4 to 0.6 and 0.8, N_{us} of specimens with the cross-section height of 1000 mm could be increased from 14,664.7 to 17,180.0 and 19,682.8 kN, respectively, which increased by 17.15% and 34.22%. K could be increased from 1662.38 to 1980.43 and 2236.21 kN·mm⁻¹, respectively, which increased by 19.13% and 34.19%. μ could be increased from 5.39 to 5.83 and 5.98, respectively, which increased by 8.15% and 11.00%. It was summarized that the N_{us} , K and μ of the specimens gradually increased with the increase in α . The specimens all showed good load-holding capacity and excellent deformation ability. Therefore, the axial compression behavior of the specimens could be improved significantly by the GFRP tube.

In summary, the N_{us} increased with the increase in f_{cc} , f_{co} , t_{gfrp} , ρ_s and α , and μ decreased with the increase in f_{cc} and f_{co} . The reasons for the above changes in the N_{us} and μ are as follows. With the increase in f_{cc} and f_{co} , the load-carrying capacity of the specimens increased while the ultimate compressive strain and transverse deformation capacity of the concrete decreased, which made the restraint effects of the GFRP tube and stirrups decrease [13,37], resulting in the increase in the N_{us} and the decrease in the μ . The core and peripheral concrete were constrained by the GFRP tube and stirrups, respectively, and with the increase in t_{gfrp} , ρ_s and ρ_s , the lateral deformation of the core concrete and the development of internal cracks became smaller, and the compressive strength of the core and peripheral concrete increased, thereby the N_{us} and μ were improved [9,37,43,44]. Moreover, the change in ρ_v had little effect on the N_{us} and μ ; this was due to the small change in the cross-sectional area of the steel bars.

6. Force Mechanism of EGCSSCs

The relationship between the longitudinal compressive strain (ϵ_1) and the circumferential strains of EGCSSCs is shown in Equation (6) [39,47], and ϵ_1 increases with the increase in the axial compression (N).

$$\begin{cases} \epsilon_f = \mu_f \epsilon_1 \\ \epsilon'_c = \mu_c \epsilon_1 \\ \epsilon_s = \mu_s \epsilon_1 \end{cases} \quad (6)$$

where ϵ'_c is the circumferential strain of the core and peripheral concrete, ϵ_f is the circumferential strain of GFRP, ϵ_s is the circumferential strain of the stirrups, μ_c is Poisson's ratio of the core and peripheral concrete, μ_f is Poisson's ratio of the GFRP, and μ_s is Poisson's ratio of the stirrups.

At the initial stage, $\mu_c < \mu_s < \mu_f$, so $\epsilon'_c < \epsilon_s < \epsilon_f$, which means that GFRP tube and stirrups have no restraint effect on core and peripheral concrete. When the longitudinal stress is approximately equal to the proportional limit of the steel bars ($\sigma_3 \approx f_p$), the

circumferential strain of steel and core and peripheral concrete is approximately equal. As the N continues to increase, $f_p < \sigma_3 < \sigma_f$ (the longitudinal stress of GFRP tube when ε_f equals ε_c), so $\varepsilon_s < \varepsilon'_c < \varepsilon_f$, which means that the circumferential deformation of the peripheral concrete is constrained by the stirrups. As the N further increases, $\sigma_f < \sigma_3$; thus, $\varepsilon_s < \varepsilon_f < \varepsilon'_c$, which means that the circumferential deformation of the core concrete is constrained by both the GFRP tube and peripheral concrete. The stress states of concrete constrained by GFRP tube and stirrups are shown in Figure 19a,b, where f_{yh} is the yield strength of the stirrup, A_{sv} is the cross-sectional area of the stirrup, f_{l0} is the circumferential stress of the stirrup, E_{gfrp} is the elastic modulus of GFRP tube, ε_g is the circumferential stress of GFRP tube, and f_{li} is the circumferential stress of GFRP tube. The stress state of EGCSSCs is shown in Figure 19c,d. The GFRP tube, core concrete, and peripheral concrete are in a three-dimensional stress state. The GFRP tube under circumferential compressive stress (σ_1), circumferential tensile stress (σ_2), and longitudinal compressive stress (σ_3) is shown in Figure 19e. The core and peripheral concrete under circumferential compressive stress (σ'_1), circumferential compressive stress (σ'_2), and longitudinal compressive stress (σ'_3) is shown in Figure 19f.

With the increase in N , the constraint effect becomes more obvious, and the middle of the specimen bulges. Both ends of the peripheral concrete are crushed locally, and the bulge at the middle of the concrete is visible. The core concrete has almost no expansion deformation due to the constraining effect of the GFRP tube and the peripheral concrete. There is not obvious expansion deformation on the GFRP tube, the longitudinal steel bars in the steel reinforcement cage are obviously yielding, and the length of stirrups at the middle of the reinforcement cage increase. Finally, the specimen exhibits outward bulge failure mode.

In order to study the stress of core concrete and peripheral concrete elements in the column section, elements A, B, C, D, E and F were successively selected in the direction far from the section center to explore the stress variation law of concrete elements in the column section from inside to outside. Figure 20a shows the distribution of six concrete elements in the middle of the SSC-1. Elements A, B and C are from core concrete, and elements D, E and F are from peripheral concrete. It can be seen from Figure 20b that from element A to element F, the peak stress gradually decreases, and the peak stress is 55.5, 51.8, 43.6, 34.7, 31.5 and 29.4 MPa, respectively, which decreases by 7.7%, 21.4%, 37.5%, 43.2% and 47.0%, and the peak strains of the elements of core concrete are much larger than those of the peripheral concrete elements. It shows that when the specimen SSC-1 reaches the ultimate axial compressive stress, the peripheral concrete reaches the peak stress earlier than the core concrete. Moreover, the confinement effect of the core concrete is greater than that of the peripheral concrete, because the core concrete is restrained by both the GFRP tube and the peripheral concrete. In this paper, the confinement effects of the core and peripheral concrete are simplified as the restraint effect coefficients of core concrete (λ) and peripheral concrete (λ_s), and $\lambda > \lambda_s$, which is consistent with the change law of the constraint effect.

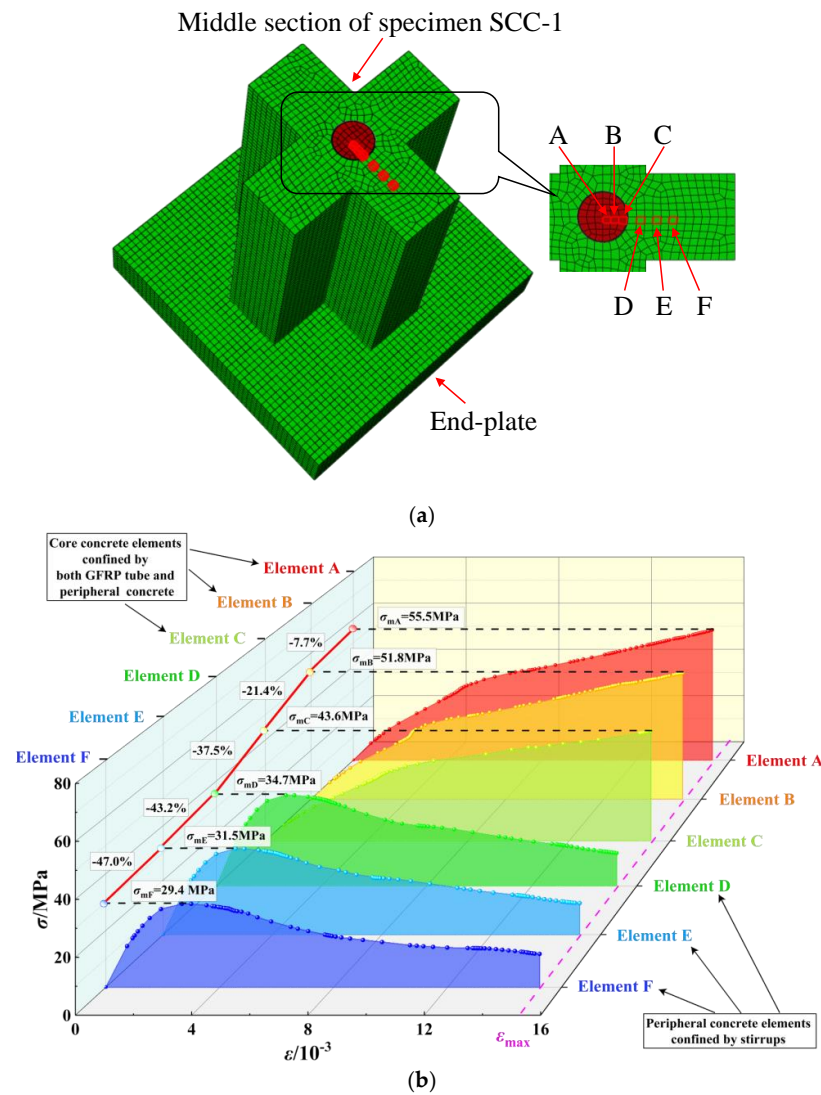


Figure 20. Stress–strain curves of concrete elements at the middle section of specimen SCC-1: (a) distribution of concrete elements; (b) stress–strain curves of elements A, B, C, D, E and F.

7. The Axial Compression-Bearing Capacity Formula of EGCSSCs

According to the analysis of the stress mechanism of the EGCSSCs, it can be concluded that the core concrete is subject to the double restraint effect of both the GFRP tube and peripheral reinforced concrete. Ghanem et al. [48] also provide a reasonable argument for this hypothesis, and it is proven that FRP has the greatest influence on the compressive stress and strain of composite columns, and stirrup is very important to the compressive strain.

From the literature [37], the bearing capacity formula of the concrete columns confined by stirrups under axial compression (N_{co}) is proposed:

$$N_{co} = A'_{co}f_{co}(1 + 1.79\lambda_s) + A_{ss}f_y \tag{7}$$

$$\lambda_s = \rho \frac{f_{yh}}{f_{c1}} \tag{8}$$

where f_{yh} is the yield strength of the stirrup. f_{c1} is the characteristic value of concrete compressive strength. A'_{co} is the cross-sectional area between the stirrup and the GFRP tube.

From the literature [27,49], the bearing capacity formula of concrete columns confined by FRP tubes under axial compression (N_{cc}) is proposed:

$$N_{cc} = A_{cc}f_{cc} \left(1 + \sqrt{\lambda} + 1.1\lambda \right) \quad (9)$$

$$\lambda_f = \mu_f \frac{f_u}{f_c} = \frac{2t_{gfrp}}{D} \frac{f_1}{f_{c1}} \quad (10)$$

where $\lambda = \lambda_s + \lambda_f$. $f_1 = E_{gfrp} \times \varepsilon_{rup}$. f_1 is the tensile strength of the GFRP tube in the circumferential direction. ε_{rup} is the fracture strain of the GFRP tube in the circumferential direction.

The axial compression-bearing capacity formula of EGCSSCs (N'_u) is obtained by using the simple superposition principle, as follows:

$$N'_u = N_{co} + N_{cc} \quad (11)$$

N'_u calculated by Equation (11) is shown in Table 6, and the comparison between N'_u and N_{us} is shown in Figure 21a. It can be seen from the figure that the $Error_{Max}$ is 17.54%, and the calculation error is large, which is not suitable for calculating the axial compression ultimate bearing capacity of EGCSSCs.

Table 6. Comparison between N'_u , N_u and N_{us} .

Specimen	μ	λ_f	λ_s	N'_u/kN	N_u/kN	N_{us}/kN	$ N'_u - N_{us} /N'_u/\%$	$ N_u - N_{us} /N_u/\%$
SSC-1	0.905	0.69	0.05	12,858.5	11,571.4	11,614.1	9.68	0.37
SSC-2	0.905	0.69	0.07	10,688.1	9607.2	10,425.5	2.46	8.52
SSC-3	0.905	0.69	0.05	14,680.7	13,220.5	13,054.1	11.08	1.26
SSC-4	0.905	0.8	0.05	12,682.2	11,411.9	10,702.2	15.61	6.22
SSC-5	0.905	0.61	0.05	13,023.1	11,720.4	12,461.8	4.31	6.33
SSC-6	0.905	1.04	0.05	12,132.5	10,914.4	10,257.2	15.46	6.02
SSC-7	0.905	0.52	0.06	13,734.5	12,364.2	13,451.2	2.06	8.79
SSC-8	0.905	0.09	0.05	12,176.2	10,954	11,092.7	8.90	1.27
SSC-9	0.905	1.73	0.05	13,459.1	12,115	12,178.3	9.52	0.52
SSC-12	0.905	0.69	0.05	14,241.2	12,822.8	13,761.7	3.37	7.32
SSC-13	0.905	0.69	0.05	14,824.0	13,350.2	12,827.5	13.47	3.92
SSC-14	0.905	0.69	0.04	19,276.4	17,379.6	17,180	10.88	1.15
SSC-15	0.905	0.53	0.06	16,548.6	14,911	15,706.7	5.09	5.34
SSC-16	0.905	0.53	0.04	23,009.7	20,758.3	19,331.5	15.99	6.87
SSC-17	0.905	0.61	0.04	19,174.7	17,287.6	16,082.3	16.13	6.97
SSC-18	0.905	0.47	0.04	20,330.7	18,333.8	18,559.5	8.71	1.23
SSC-19	0.905	0.79	0.04	17,784.4	16,029.4	14,664.7	17.54	8.51
SSC-20	0.905	0.4	0.05	21,375.8	19,279.6	19,682.8	7.92	2.09
SSC-21	0.905	0.07	0.04	19,117.3	17,235.7	15,950.4	16.57	7.46
SSC-22	0.905	1.1	0.04	20,885.1	18,835.5	18,243.5	12.65	3.14
SSC-25	0.905	0.53	0.04	21,650.2	19,527.9	19,096.7	11.79	2.21
SSC-26	0.905	0.53	0.04	22,225.5	20,048.6	21,500	3.26	7.24

According to the force mechanism of EGCSSCs, it can be seen that the core concrete and peripheral concrete cannot reach peak stress at the same time, because ρ_v has little effect on the axial compression-bearing capacity. Therefore, the bearing capacity provided by the steel bar is ignored, and the calculation formula for the ultimate bearing capacity of EGCSSCs under axial compression (N_u) is established by introducing the reduction coefficient (η), which could be expressed as follows:

$$N_u = \eta [N_{co} + A'_{co}f_{co}(1 + 1.79\lambda_s)] \quad (12)$$

The global optimization algorithm (Leveberg–Marquardt) of 1st Opt software is used to determine the value of η . The formula reaches the convergence criterion, and η is determined to be 0.905 after 17 iterations of operation, $R = 0.95$, and $R^2 = 0.91$. Finally, the axial compression-bearing capacity formula of EGCSSCs is obtained by substituting the value of η into Equation (12), which is shown in Equation (12).

$$N_u = 0.905 \left[A_{co}f_{co}(1 + 1.79\lambda_s) + A_{cc}f_{cc}(1 + \sqrt{(\lambda_f + \lambda_s)} + 1.1(\lambda_f + \lambda_s)) \right] \quad (13)$$

Table 6 lists the N_u calculated by Equation (13) and N_{us} of EGCSSCs. Figure 21b compares N_u and N_{us} . The $Error_{Max}$ between the N_u and N_s was 8.79%, which could meet the requirements of practical engineering.

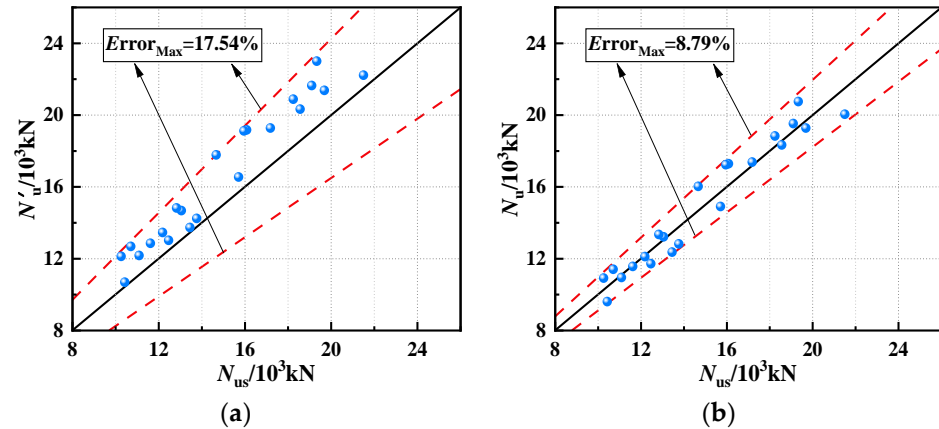


Figure 21. Comparison between N'_u , N_u and N_{us} . (a) Comparison between N_u and N_{us} . (b) Comparison between N_u and N_{us} .

8. Conclusions

In order to investigate the mechanical behavior of EGCSSCs under axial load, 27 full-scale EGCSSCs were designed with varying parameters: axial compressive strength of core concrete (f_{cc}), axial compressive strength of peripheral concrete (f_{co}), thickness of GFRP tube (t_{grp}), ratio of longitudinal reinforcement (ρ_v), stirrup ratio (ρ_s) and GFRP ratio in the cross-section (α). Then, 27 EGCSSCs finite element models were established by ABAQUS finite element software. Based on the range of parameters in this paper, the conclusions could be drawn as follows:

- (1) Based on the simplified bilinear constitutive model of steel bars and stirrups, and the nonlinear constitutive models of core and peripheral concrete considering restraint, and the reasonable FEM method, 27 finite element models of composite columns were numerically simulated by ABAQUS finite element software.
- (2) All specimens showed excellent load-carrying capacity and good ductility. The axial compression behavior of EGCSSCs increased significantly with the increase in f_{cc} , f_{co} , t_{grp} , ρ_s and α . However, the change in ρ_v had little effect on its axial compression behavior. Moreover, with the existence of GFRP core columns, the N_{us} and μ of the columns were increased by 11.61% and 140.86%. In addition, K increased with the increase in f_{cc} , f_{co} , t_{grp} and α , and the largest increments were 23.99%, 50.54%, 21.77% and 34.19%, respectively. μ decreased with the increase in f_{cc} and f_{co} , which decreased by 14.05% and 40.82%, respectively.
- (3) The restraint effects on the element of EGCSSCs distributed along the circumferential direction were different, and the maximum stress of concrete elements gradually decreased from the center of EGCSSCs to the edges, indicating that the restraint effect on the core concrete was larger than that on the peripheral concrete. Moreover, the peripheral concrete reached peak stress earlier than the core concrete, and the peak stress of the peripheral concrete elements was close to that of ordinary concrete. In this paper, the confinement effects of core and peripheral concrete were simplified as the restraint effect coefficients of core concrete (λ) and peripheral concrete (λ_s), and $\lambda > \lambda_s$, which was consistent with the change law of the constraint effect. Because the core and peripheral concrete could not reach the peak stress at the same time, the bearing capacity of the column had a certain loss.

- (4) The axial compression-bearing capacity formula of EGCSSCs was proposed by introducing the reduction coefficient (η). The global optimization algorithm (Leveberg–Marquardt) of 1st Opt software was used to determine the value of η . The $Error_{Max}$ between the calculation results and simulation results was 8.79%, which could meet the engineering accuracy requirements.

In this paper, the influence of parameters on the mechanical behavior of EGCSSCs under axial compression was carried out. However, the axial compressive mechanical behavior was also affected by the interaction between parameters. Therefore, in the future, statistical analysis methods can be used to study the main effects and interaction effects. Future research in this area can include the effect of eccentric loading on axial-bearing capacity. Moreover, in addition to composite columns, this type of composite beam can also be included in the study, using the finite element analysis to predict compressive strength and flexural strength.

The authors believe that the axial-bearing capacity formula based on the finite element model simulation analysis is simple to calculate and meets the error requirements of engineering, which can provide a design basis for engineers' practice to a large extent.

Author Contributions: Conceptualization, J.J.; software, J.J. and J.L.; validation, H.R. and Q.W.; writing—original draft, J.J., L.J. and J.L.; writing—review and editing, X.W., Q.W. and L.H.; resources, J.J.; data curation, Z.Z.; supervision, J.J.; project administration, J.J.; funding acquisition, J.J. All authors have read and agreed to the published version of the manuscript.

Funding: This research was funded by [General Project of National Natural Science Foundation of China] grant number [52178143], [Joint Guidance Project of Natural Science Foundation of Heilongjiang Province] grant number [LH 2020E018]), [China-Pakistan Belt and Road Joint Laboratory on Smart Disaster Prevention of Major Infrastructure] grant number [2022CPBRJL-05], [2021 Social Science Development Research Project of Hebei Province] grant number [20210301135]), [Humanities and Social Science Research Project of Higher Education Institutions of Hebei Province] grant number [SQ2021115], [The Guided Innovation Fund of Northeast Petroleum University] grant number [2020YDL-02] and [Guiding Science and Technology Project of Daqing City] grant number [zd-2021-40].

Institutional Review Board Statement: Not applicable.

Informed Consent Statement: Not applicable.

Data Availability Statement: The data used to support the findings of this study are included within the article.

Conflicts of Interest: The authors declare that the research was conducted in the absence of any commercial or financial relationships that could be construed as a potential conflict of interest.

Glossary

A_{co}/mm^2	section area of the EGCSSCs/
A'_{co}/mm^2	cross-sectional area between the stirrup and the GFRP tube
A_{ss}/mm^2	section area of longitudinal steel bars
A_{sv}/mm^2	cross-sectional area of the stirrup
B/mm	cross-section height of EGCSSCs
B_1/mm	width of the specimens in Table 4
b_{cor}/mm	length of the core concrete in Table 4
D/mm	diameter of the GFRP tube
D_c/mm	diameter of the CFRP tube
d_s/mm	diameter of the stirrup
E_1/MPa	elastic modulus of GFRP in the tangential direction
E_2/MPa	elastic modulus of GFRP in the normal direction
E'_2/MPa	initial elastic modulus of concrete
E_c/MPa	elastic modulus of concrete
E_{gfrp}/MPa	elastic modulus of the GFRP tube

σ_0, f_c /MPa	compressive strength of the concrete
f_{cc} /MPa	axial compressive strength of core concrete
f'_{cc} /MPa	compressive strengths of the confined concrete
f_{co} /MPa	axial compressive strength of peripheral concrete
f'_{co} /MPa	compressive strengths of the unconfined concrete
f_{co1} /MPa	axial compressive strength of plain concrete
f_{cu} /MPa	cube compressive strength of the concrete
f_{c1} /MPa	characteristic value of concrete compressive strength.
f_1 /MPa	tensile strength of the GFRP tube in the circumferential direction
f_{li} /MPa	circumferential stress of GFRP tube
f_{lo} /MPa	circumferential stress of the stirrup
f_{sy} /MPa	yield strength of steel
f_y /MPa	yield strength of the rectangular steel tube or the steel bar
f_{yh} /MPa	yield strength of the stirrup
H /mm	height of the EGCSSCs
G_{12} /MPa	shear modulus of GFRP
$K/\text{kN}\cdot\text{mm}^{-1}$	initial stiffness of EGCSSCs
L /mm	cross-section width of EGCSSCs
l /mm	length of stirrup
N_{cc} /kN	ultimate bearing capacity of EGCSSCs
N_{co} /kN	ultimate bearing capacity of EGCSSCs
N_s /kN	ultimate bearing capacity obtained by simulations
N_t /kN	ultimate bearing capacity obtained by experiments
N_u /kN	ultimate bearing capacity of EGCSSCs calculated by Equation (13)
N'_u /kN	ultimate bearing capacity of EGCSSCs calculated by Equation (11)
N_{us} /kN	ultimate bearing capacity of simulated EGCSSCs
R /-	correlation coefficient
R^2 /-	R-square
s /mm	spacing of the stirrups
s_1 /mm	stirrup spacing in the densification zone
S_1 /mm	stirrup spacing in densification zone in Table 4
T /-	descending parameter
t_c /mm	thickness of the CFRP tube
t_{grfp} /mm	thickness of GFRP tube
t_s /mm	thickness of the steel tube
t_r /mm	relative thickness adjacent layers of GFRP
ν_{12} /-	Poisson's ratio of GFRP
X_c /MPa	longitudinal compressive strength of GFRP
X_T /MPa	longitudinal tensile strength of GFRP
Y_c /MPa	transverse compressive strength of GFRP
μ /-	ductility index of EGCSSCs
Y_T /MPa	transverse tensile strength of GFRP
μ_c /-	Poisson's ratio of the core and peripheral concrete
μ_s /-	Poisson's ratio of the stirrups
μ_f /-	Poisson's ratio of the GFRP
ε_0 /-	peak strain corresponding to σ_0
ε_1 /-	longitudinal compressive strain
ε_c /-	strain corresponding to σ_c
ε'_c /-	circumferential strain of the core and peripheral concrete
ε'_{cc}	ultimate strain of concrete
ε_{co1} /-	peak strain corresponding to f_{co1}
ε_f /-	circumferential strain of GFRP
ε_g /-	circumferential stress of GFRP tube
ε_p /-	peak tensile strain corresponding to σ_p
ε_{rup} /-	fracture strain of the GFRP tube in the circumferential direction
ε_s /-	circumferential strain of the stirrups
ε_{sy} /-	yield strain of steel
σ_1 /MPa	circumferential compressive stress of GFRP tube
σ_2 /MPa	circumferential tensile stress
σ_3 /MPa	longitudinal compressive stress
σ'_1 /MPa	circumferential compressive stress of the core and peripheral concrete
σ'_2 /MPa	circumferential compressive stress of the core and peripheral concrete

σ'_3 /MPa	longitudinal compressive stress of the core and peripheral concrete
σ_c /MPa	tensile stress of concrete
σ_p /MPa	peak tensile stress of concrete
θ /MPa	relative laying angle adjacent layers of GFRP
Δ_u /mm	ultimate displacement of EGCSSCs
Δ_y /mm	yielding displacement of EGCSSCs.
η /-	reduction coefficient
ρ_v /%	ratio of longitudinal reinforcement
ρ_s /%	stirrup ratio
α /-	GFRP ratio in the cross-section
λ_f /-	restraint effect coefficients of GFRP tubes
λ_s /-	restraint effect coefficients of stirrups
λ_v /-	stirrup characteristic value

References

- Zhang, Z.; Shi, G.; Wang, S.; Zhou, L. Investigation on buckling behavior of T-shaped box-T section columns under axial load. *Eng. Struct.* **2022**, *254*, 113904. [[CrossRef](#)]
- Jahami, A.; Temsah, Y.; Khatib, J.; Baalbaki, O. The behavior of CFRP strengthened RC beams subjected to blast loading. *Mag. Civ. Eng.* **2021**, *103*, 10309.
- Ibrahim, M.; Wakjira, T.; Ebead, U. Shear strengthening of reinforced concrete deep beams using near-surface mounted hybrid carbon/glass fibre reinforced polymer strips. *Eng. Struct.* **2020**, *210*, 110412. [[CrossRef](#)]
- Wakjira, T.G.; Al-Hamrani, A.; Ebead, U.; Alnahhal, W. Shear capacity prediction of FRP-RC beams using single and ensemble Explainable Machine learning models. *Compos. Struct.* **2022**, *287*, 115381. [[CrossRef](#)]
- Wakjira, T.G.; Abushanab, A.; Ebead, U.; Alnahhal, W. FAI: Fast, accurate, and intelligent approach and prediction tool for flexural capacity of FRP-RC beams based on super-learner machine learning model. *Mater. Today Commun.* **2022**, *33*, 104461. [[CrossRef](#)]
- Vedernikov, A.; Minchenkov, K.; Gusev, S.; Sulimov, A.; Zhou, P.; Li, C.; Xian, G.; Akhatov, I.; Safonov, A. Effects of the Pre-Consolidated Materials Manufacturing Method on the Mechanical Properties of Pultruded Thermoplastic Composites. *Polymers* **2022**, *14*, 2246. [[CrossRef](#)]
- Fedulov, B.N.; Safonov, A.A.; Sergeichev, I.V.; Ushakov, A.E.; Klenin, Y.G.; Makarenko, I.V. Strength Analysis and Process Simulation of Subway Contact Rail Support Bracket of Composite Materials. *Appl. Compos. Mater.* **2016**, *23*, 999–1013. [[CrossRef](#)]
- Cakiroglu, C.; Islam, K.; Bekdaş, G.; Isikdag, U.; Mangalathu, S. Explainable machine learning models for predicting the axial compression capacity of concrete filled steel tubular columns. *Constr. Build. Mater.* **2022**, *356*, 129227. [[CrossRef](#)]
- Rodsın, K.; Hussain, Q.; Suparp, S.; Nawaz, A. Compressive behavior of extremely low strength concrete confined with low-cost glass FRP composites. *Case Stud. Constr. Mater.* **2020**, *13*, e00452. [[CrossRef](#)]
- Bedon, C.; Rajčić, V. Textiles and Fabrics for Enhanced Structural Glass Facades: Potentials and Challenges. *Buildings* **2019**, *9*, 156. [[CrossRef](#)]
- Moskaleva, A.; Safonov, A.; Hernández-Montes, E. Fiber-Reinforced Polymers in Freeform Structures: A Review. *Buildings* **2021**, *11*, 481. [[CrossRef](#)]
- Ji, J.; Zeng, W.; Wang, R.; Ren, H.; Zhang, L.; Liu, Y.; Jiang, L.; He, L.; Lin, Y.; Yu, C. Bearing Capacity of Hollow GFRP Pipe-Concrete-High Strength Steel Tube Composite Long Columns Under Eccentric Compression Load. *Front. Mater.* **2021**, *8*, 768877. [[CrossRef](#)]
- Ji, J.; He, L.; Jiang, L.; Ren, H.; Ni, S.; Wang, Z.; Li, Y.; Yu, C.; Lin, Y. Seismic Behavior of GFRP Tube Reactive Powder Concrete Composite Columns With Encased Steel. *Front. Mater.* **2021**, *8*, 793392. [[CrossRef](#)]
- Li, S.; Chan, T.-M.; Young, B. Behavior of GFRP-concrete double tube composite columns. *Thin-Walled Struct.* **2022**, *178*, 10940. [[CrossRef](#)]
- Han, L.H. *Concrete Filled Steel Tube Structures: Theory and Practice*; Science Press: Beijing, China, 2007.
- Wang, F.-C.; Han, L.-H. Analytical behavior of special-shaped CFST stub columns under axial compression. *Thin-Walled Struct.* **2018**, *129*, 404–417. [[CrossRef](#)]
- Liu, X.; Xu, C.; Liu, J.; Yang, Y. Research on special-shaped concrete-filled steel tubular columns under axial compression. *J. Constr. Steel Res.* **2018**, *147*, 203–223. [[CrossRef](#)]
- Liu, X.; Liu, J.; Yang, Y.; Cheng, G.; Lanning, J. Resistance of special-shaped concrete-filled steel tube columns under compression and bending. *J. Constr. Steel Res.* **2020**, *169*, 106038. [[CrossRef](#)]
- Chen, Z.; Mo, L.; Li, S.; Liang, Y.; Xu, D. Seismic behavior of steel reinforced concrete L-shaped columns under compression-bending-shear-torsion combined action. *J. Build. Eng.* **2021**, *42*, 102498. [[CrossRef](#)]
- Hassam, M.; Guo, L.; Wang, Y. Experimental and numerical investigation of cross-shaped stub CFSTs under axial compression. *Mag. Concr. Res.* **2021**, *73*, 1225–1240. [[CrossRef](#)]
- Wang, Y.; Guo, L.; Li, H. L-shaped steel-concrete composite columns under axial load: Experiment, simulations and design method. *J. Constr. Steel Res.* **2021**, *185*, 106871. [[CrossRef](#)]

22. Ji, J.; Xu, Z.; Jiang, L.; Yuan, C.; Zhang, Y.; Zhou, L.; Zhang, S. Nonlinear Buckling Analysis of H-Type Honeycombed Composite Column with Rectangular Concrete-Filled Steel Tube Flanges. *Int. J. Steel Struct.* **2018**, *18*, 1153–1166. [[CrossRef](#)]
23. Ji, J.; Li, Y.; Jiang, L.; Ren, H.; Wang, Q.; Zhang, L.; He, L.; Zhang, Z. Flexural behavior of composite beams with concrete filled steel tube flanges and honeycombed steel webs. *Front. Mater.* **2022**, *9*, 991584. [[CrossRef](#)]
24. Ji, J.; Yu, C.; Jiang, L.; Zhan, J.; Ren, H.; Hao, S.; Fan, S.; Jiang, L.; Lin, Y.; He, L. Bearing Behavior of H-Shaped Honeycombed Steel Web Composite Columns with Rectangular Concrete-Filled Steel Tube Flanges under Eccentric Compression Load. *Adv. Civ. Eng.* **2022**, *2022*, 2965131. [[CrossRef](#)]
25. Ji, J.; Lin, Y.; Jiang, L.; Li, W.; Ren, H.; Wang, R.; Wang, Z.; Yang, M.; Yu, C. Hysteretic Behavior of H-Shaped Honeycombed Steel Web Composite Columns with Rectangular Concrete-Filled Steel Tube Flanges. *Adv. Civ. Eng.* **2022**, *2022*, 1546263. [[CrossRef](#)]
26. Li, H.; Tong, Y.; Yin, J.; Zhang, H.; Yan, C. Study on Axial Compression Behavior of Cross-Shaped and L-Shaped Multi-cavity Concrete-Filled Steel Tube Special Shaped Column. *Int. J. Steel Struct.* **2022**, *22*, 153–175. [[CrossRef](#)]
27. Lam, L.; Teng, J. Design-oriented stress-strain model for FRP-confined concrete. *Constr. Build. Mater.* **2003**, *17*, 471–489. [[CrossRef](#)]
28. Huang, L.; Sun, X.; Yan, L.; Kasal, B. Impact behavior of concrete columns confined by both GFRP tube and steel spiral reinforcement. *Constr. Build. Mater.* **2017**, *131*, 438–448. [[CrossRef](#)]
29. Sun, H.; Jia, M.; Zhang, S.; Wang, Y. Study of buckling-restrained braces with concrete infilled GFRP tubes. *Thin-Walled Struct.* **2019**, *136*, 16–33. [[CrossRef](#)]
30. Ren, F.; Liang, Y.; Ho, J.; Lai, M. Behaviour of FRP tube-concrete-encased steel composite columns. *Compos. Struct.* **2020**, *241*, 112139. [[CrossRef](#)]
31. Hui, C.; Li, Y.; Zhou, Z.; Hai, R. Behavior of concrete-filled GFRP tube columns under cyclic axial compression. *Constr. Build. Mater.* **2021**, *294*, 123566. [[CrossRef](#)]
32. Long, Y.-L.; Li, W.-T.; Dai, J.-G.; Gardner, L. Experimental study of concrete-filled CHS stub columns with inner FRP tubes. *Thin-Walled Struct.* **2018**, *122*, 606–621. [[CrossRef](#)]
33. Wang, Z.; Feng, P.; Zhao, Y.; Yu, T. FRP-confined concrete core-encased rebar for RC columns: Concept and axial compressive behavior. *Compos. Struct.* **2019**, *222*, 110915. [[CrossRef](#)]
34. Chen, J.; Zhu, Y.; Wang, F.; Feng, B. Experimental and analytical study of hollow section concrete-filled GFRP tubes in bending. *Thin-Walled Struct.* **2022**, *177*, 109297. [[CrossRef](#)]
35. Yuan, J.-S.; Xin, Z.; Gao, D.; Zhu, H.; Chen, G.; Hadi, M.N.; Zeng, J.-J. Behavior of hollow concrete-filled rectangular GFRP tube beams under bending. *Compos. Struct.* **2022**, *286*, 115348. [[CrossRef](#)]
36. Su, J.; Wang, J.; Li, Z.; Liang, X. Effect of reinforcement grade and concrete strength on seismic performance of reinforced concrete bridge piers. *Eng. Struct.* **2019**, *198*, 109512. [[CrossRef](#)]
37. Qian, J.R.; Cheng, L.; Zhou, D. Behavior of axially loaded concrete columns confined with ordinary hoops. *J. Tsinghua Univ. Sci. Technol.* **2002**, *42*, 1369–1373.
38. GB50010-2010. Chinese Code for Design of Concrete Structure. China Construction Industry Press: Beijing, China, 2010.
39. Ji, J.; Wang, W.; Jiang, L.; Ren, H.; Wang, Q.; Xuan, W.; Liu, Y. Bearing Capacity of UHPC-Filled High-Strength Elliptical Steel Tube Composite Columns with Encased High-Strength H-Shape Steel Subjected to Eccentric Load. *Buildings* **2022**, *12*, 1272. [[CrossRef](#)]
40. Bai, W.; Li, Y.; Ji, J.; Liu, Y.; Zhang, L.; Wang, R.; Jiang, L.; He, L. Axial Compression Behavior of Symmetrical Full-Scale Concrete Filled Double Skin Steel Tube Stub Columns. *Symmetry* **2022**, *14*, 223. [[CrossRef](#)]
41. Che, Y.; Wang, T.D.; Ban, S.L.; Song, Y.P. Size effect on behavior of concrete confined by stirrups under axial compression. *J. Build. Struct.* **2013**, *34*, 118–123.
42. Radnic, J.; Markic, R.; Harapin, A.; Matesan, D.; Baloevic, G. Stirrup effects on compressive strength and ductility of confined concrete columns. *World J. Eng.* **2013**, *10*, 497–506. [[CrossRef](#)]
43. Li, G.C.; Shi, J.J.; Yang, Z.J.; Zhao, Q.H. Experimental Study on Middle Long Columns of High Strength Concrete Filled Square Steel Tube with Inner CFRP Circular Tube under Axial Compressive Load. *J. Shenyang Archit. Civ. Eng. Univ. Nat. Sci.* **2010**, *26*, 47–51.
44. Li, G.C.; Luo, J.L.; Nie, Y.; Ren, Q.S. Experiment on Performance of High-strength Concrete-filled Square Steel Tube Long Columns with Inner CFRP Circular Tube under Axial Compression. *J. Archit. Civ. Eng.* **2009**, *26*, 21–25.
45. Ji, J. *Research on Seismic Performance and Design Method of Jacketing Steel Reinforced Concrete Frame Prestressed with Bonded Tendons*; Harbin Institute of Technology: Harbin, China, 2008.
46. Ji, J.; Zeng, W.; Jiang, L.; Bai, W.; Ren, H.; Chai, Q.; Zhang, L.; Wang, H.; Li, Y.; He, L. Hysteretic Behavior on Asymmetrical Composite Joints with Concrete-Filled Steel Tube Columns and Unequal High Steel Beams. *Symmetry* **2021**, *13*, 2381. [[CrossRef](#)]
47. Rong, Q.; Hou, X.; Ge, C. Quantifying curing and composition effects on compressive and tensile strength of 160–250 MPa RPC. *Constr. Build. Mater.* **2020**, *241*, 117987. [[CrossRef](#)]
48. Ghanem, S.Y.; Elgazzar, H. Predicting the behavior of reinforced concrete columns confined by fiber reinforced polymers using data mining techniques. *SN Appl. Sci.* **2021**, *3*, 170. [[CrossRef](#)]
49. Teng, J.G.; Yu, T.; Wong, Y.L.; Dong, S.L. Hybrid FRP-concrete-steel tubular columns: Concept and behavior. *Constr. Build. Mater.* **2007**, *21*, 846–854. [[CrossRef](#)]